Available online at www.sciencedirect.com
SCIENCE DIRECT
Journal of volcanology and geothermal research
ELSEVIER
Journal of Volcanology and Geothermal Research 155 (2006) 201–226
www.elsevier.com/locate/jvolgeores

# The 2001–2004 dome-forming eruption of Shiveluch volcano, Kamchatka: Observation, petrological investigation and numerical modelling

O. Dirksen [a], M.C.S. Humphreys [b,*], P. Pletchov [c], O. Melnik [b,d], Y. Demyanchuk [a], R.S.J. Sparks [b], S. Mahony [b]

[a] *Institute of Volcanology and Seismology, Petropavlovsk-Kamchatsky, 9 Piip Blvd, 683006, Petropavlovsk-Kamchatsky, Russia*
[b] *Department of Earth Sciences, University of Bristol, Wills Memorial Building, Queen's Road, Bristol, BS8 1RJ, UK*
[c] *Geological Department, Moscow State University, MSU, Vorobievy Gory, MSU, 119899, Moscow, Russia*
[d] *Institute of Mechanics, Moscow State University, 1-Michurinskii prosp., 119192, Moscow, Russia*

Received 24 October 2005; received in revised form 8 February 2006; accepted 16 March 2006
Available online 5 June 2006

**Abstract**

There have been three episodes of lava dome growth at Shiveluch volcano, Kamchatka since the Plinian explosive eruption in 1964. The episodes in 1980–1981, 1993–1995 and 2001–2004 have discharged at least 0.27 $km^3$ of silicic andesite magma. A time-averaged mean extrusion rate of 0.2 $m^3/s$ is thus estimated for the last 40 years. Here the 2001–2004 activity is described and compared with the earlier episodes. The recent activity involved three pulses in extrusion rate and a transition to ongoing lava extrusion. Estimated magma temperatures are in the range 830 to 900 °C, with 850 °C as the best estimate, using the plagioclase −amphibole phenocryst assemblage and Fe−Ti oxides. Melt inclusions in amphibole and plagioclase have maximum water contents of 5.1 wt.%, implying a minimum pressure of ~155 MPa for water-saturated conditions. The magma chamber depth is estimated to be about 5–6 km or more, a result consistent with geophysical data. The thicknesses of opx–mt–amph reaction rims on olivine xenocrysts are used to estimate the residence time of olivine crystals in the shallow chamber in the range 2 months to 4 years, suggesting replenishment of deeper magma into the shallow chamber contemporaneous with eruption. The absence of decompression-driven breakdown rims around amphiboles indicates ascent times of less than 7 days. Volcanological observations of the start of the 2001–2004 episode suggest approximately 16 days for the ascent time and a conduit equivalent to a cylinder of diameter approximately 53–71 m. Application of a conduit flow model indicates that the magma chamber was replenished during the 2001–2004 eruption, consistent with the results of olivine reaction rims, and that the chamber has an estimated volume of order 7 $km^3$.


*Keywords:* Shiveluch; lava dome; petrology; volcanic eruption; conduit flow; numerical model

## 1. Introduction

The Shiveluch volcanic complex (56°38′N, 161°19′E) is located in the northern part of Central Kamchatka depression in the boundary zone of the Aleutian and

* Corresponding author. Fax: +44 117 925 3385.
*E-mail address:* madeleine.humphreys@bristol.ac.uk (M.C.S. Humphreys).

0377-0273/$ - see front matter © 2006 Elsevier B.V. All rights reserved.
doi:10.1016/j.jvolgeores.2006.03.029

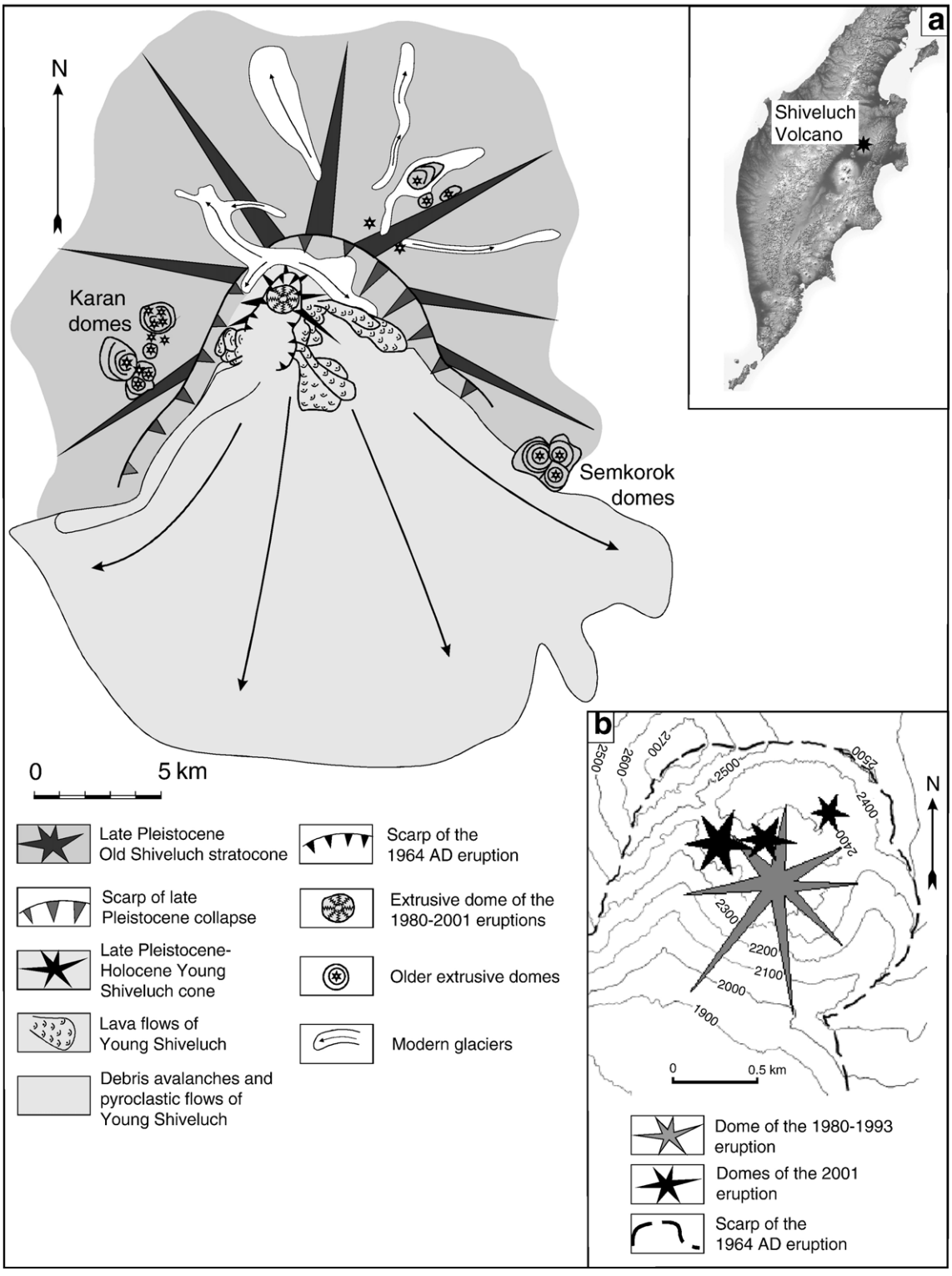


Fig. 1. Geological map of Shiveluch volcano. Insets: (a) Location of the volcano, (b) position of the domes of the 2001–2004 eruption.

Kurile–Kamchatka island arcs (Fig. 1a). Shiveluch is the northernmost active volcano of the Kamchatka peninsula. The volcano has been very active during the Holocene with over 60 tephra fall deposits identified, numerous lava dome extrusions, and several edifice collapses producing debris avalanches. The most recent stage of volcanic activity started with a Plinian eruption in 1964, and was followed by three episodes of lava dome extrusion between 1964 and the present.

This paper describes the latest dome extrusion episode (2001–2004) which is still ongoing, with some comparison with the previous episodes. The eruption is documented, including data on dome volume, extrusion rate and a series of more than 900 minor explosions. The petrology and geochemistry of the new lava dome is described and used to infer conditions in the magma chamber and during magma ascent. The study uses reaction rims around olivine xenocrysts, and the absence of decompression-driven breakdown rims on amphibole, to constrain magma ascent times. Models of magma flow along conduits (after Melnik and Sparks, 2005) are applied, in order to interpret the observations in terms of eruption dynamics and to estimate magma chamber volume.

## 2. Geological background

The modern volcanic edifice consists of two main parts: Old Shiveluch and Young Shiveluch (Fig. 1). Old Shiveluch (the major summit, height 3335 m a.s.l.) represents the remains of a giant stratovolcano with a diameter of approximately 45–50 km, including the surrounding flanks of fluvial and fluvioglacial volcanoclastic plains (Melekestsev et al., 1991). There is limited information on the geology of Old Shiveluch (Menyailov, 1955; Melekestsev et al., 1991; Belousov et al., 1999). The oldest rocks of the Old Shiveluch cone (50 to 60 ka) are represented by thick sequences of andesitic pyroclastic flows deposits, mainly of block-and-ash flow type. This core is overlain by pyroclastic deposits, lava flows and domes of amph–plag–px andesite and plag–px basaltic andesites (Melekestsev et al., 1991). The southern part of the volcano was removed by a huge landslide, which formed an arcuate scarp broadly opened to the south (Fig. 1). The age of this event is older than 23–24 ka (Melekestsev et al., 1991; Braitseva et al., 1995). Menyailov (1955) and Melekestsev et al. (1991) relate this feature to the Late Pleistocene caldera-forming eruption ca. 30 ka. However, associated pyroclastic deposits have not been recognised. Such an asymmetric feature together with a debris avalanche deposit is more consistent with a sector collapse origin. The debris avalanche deposit, with a volume of approximately 50–60 $km^3$, is preserved as a hummocky plain at the southern sector of volcano beyond the field of Holocene volcanoclastic deposits (Melekestsev et al., 1991).

There is a gap in the geological sequence between the deposits at ~30 ka and volcanic products of Holocene age, probably due to strong glaciation rather than the absence of volcanic activity. Holocene volcanism developed in the northwest sector of the landslide scarp to build the Young Shiveluch edifice (Fig. 1). Young Shiveluch is composed of multiple coalesced extrusive domes, surrounded by volcanic breccias and short but thick (up to 100 m) lava flows. Holocene activity has been characterised by at least 60 explosive eruptions with volumes in excess of 0.1 $km^3$, alternating with periods of dome growth accompanied by weak phreatic and phreato-magmatic explosive eruptions (Ponomareva et al., 1998). Several satellite domes were emplaced on the flanks of the volcano away from Young Shiveluch (Fig. 1); these include the Late Pleistocene Semkorok domes at the southeastern base and the Holocene Karan domes on the western slope of Old Shiveluch. The recorded history of Shiveluch eruptions goes back only as far as 300 years; older eruptions have been dated by $^{14}C$ and tephrochronology (Melekestsev et al., 1991; Ponomareva et al., 1998). Several of the largest explosive eruptions (with volumes of erupted products ca. 4–5 $km^3$) were accompanied by directed blasts, debris avalanches and formation of pyroclastic flows (Melekestsev et al., 1991; Ponomareva et al., 1998; Belousov et al., 1999). Tephra fall deposits covered significant areas of North Kamchatka and the surrounding seas. These well-dated tephra layers provide chronological horizons to distances as far as 200–300 km from the source (Braitseva et al., 1995, 1997a,b; Ponomareva et al., 1998; Pevzner et al., 1998).

The most recent major explosive eruption of Shiveluch occurred on 12 November 1964 (Belousov, 1995; Firstov et al., 1994). The Plinian eruption created a twin horseshoe crater, open to the south, in the Young Shiveluch edifice, and formed a widespread debris avalanche (1.5 $km^3$) and pyroclastic flow deposits. The tephra layer covered a vast area to the east–southeast of the volcano and reached the Kommandor islands, 300 km southeast of the volcano. Debris avalanche material and pyroclastic flows covered more than 100 $km^2$ on the southern flanks of the volcano. The volume of juvenile material erupted is estimated to be about 0.6–0.8 $km^3$ (Ponomareva et al., 1998).

## 3. Volcanic activity after the 1964 eruption

Volcanic activity after 1964 is summarised in Fig. 2 in terms of the volumes of lava extruded and extrusion rate. The main episodes are described below.

### 3.1. 1980–1981 eruption

Shortly after the 1964 eruption, the crater floor was uplifted by up to 25 m over an area 300 m in diameter. The centre of uplift then subsided to form a pit crater. Several small explosion craters formed within this pit crater, which was the main focus of fumarolic activity. Several hot areas were situated on the walls and floor of the crater. Fumarolic activity declined gradually: the temperature of the main fumarole decreased from 240–300 °C in 1966–1968 to 98 °C in 1972 (Melekestsev et al., 2004). In September 1979 the main fumarole temperature increased to 216 °C. The composition of gas condensate in this fumarole also changed. Cl increased from 130 to 1500 mg/l, B from 4 to 180 mg/l, $NH_4$ from 0 to 11 mg/l, while S decreased from 1520 to 600 mg/l (Kirsanova T.P., personal communication). Gas compositions were similar to those measured after the 1964 eruption. On 3 July 1980, several small crater lakes disappeared, suggesting either ground dilation due to deformation or drying out of the ground water system as a result of magma ascent.

An extrusive dome started to grow in the 1964 crater on 23 August 1980, located at the same place as the area of uplift in 1964. No precursors of seismicity or explosive activity were recorded (Gorelchik et al., 1997), which suggests that magma was located at shallow depths prior to the eruption onset. During the next 2 months the extrusion rate of the magma was relatively high with a maximum of 3.2 $m^3/s$ in mid-September (Fig. 2). The extrusion rate then declined to 0.3 $m^3/s$ by 5 March 1981. Extrusion of the dome was accompanied by small explosions, and by partial dome collapses which generated rock-falls and small pyroclastic flows (Gorelchik et al., 1997). The active growth of the dome ceased at the end of 1981 when the dome

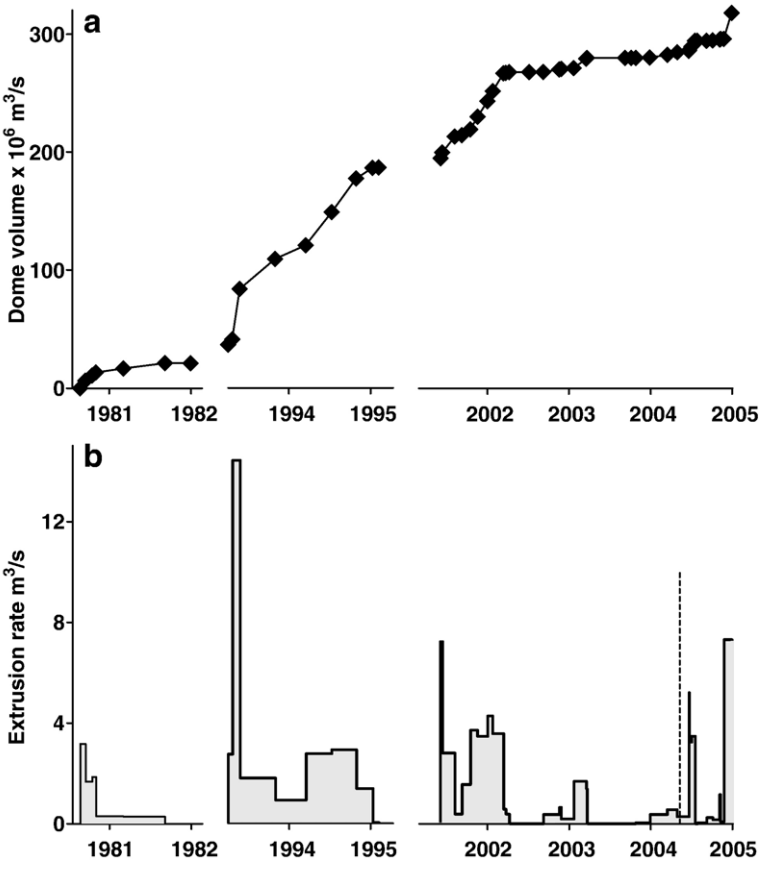


Fig. 2. Data on the cumulative volume of the lava dome (a) and extrusion rate (b) are shown against time for the 1980 to 2005 period for Shiveluch Volcano. Dashed line indicates explosive eruption on 9 May 2004, marking a change in eruptive style (see text for details).

reached a height of 200 m, with an estimated volume of $21 \times 10^6$ m$^3$ and an average extrusion rate of 0.5 m$^3$/s over the 1980–1981 period.

### 3.2. 1982–1992 activity

From the end of 1981 to 1984 only fumarolic activity was observed. Weak explosive activity within the dome began in March 1984 and increased from 4–5 explosions in 1984, through 35–40 in 1987, to 50 in 1990 (Zharinov et al., 1995). Initially, explosive craters were situated both on the dome and at its foot. Later explosive activity concentrated at two explosive craters on top of the dome. In 1989 these craters coalesced to form a larger one (320 × 220 m) up to 100 m in depth (Melekestsev et al., 2004). Further explosive activity occurred mainly through this crater. In 1990 the activity became more vigorous with some explosions accompanied by pyroclastic flows, which travelled up to 2 km. During 1991–1992 the size of the heated areas increased, new arcuate fractures were observed, and new fumaroles developed.

### 3.3. 1993–1995 eruption

At the beginning of April 1993 seismicity started to increase rapidly (Gorelchik et al., 1997). A new eruption started on 20 April 1993 when several new extrusive spines were observed at the 1980–1981 dome. On 22 April a large explosion occurred with the eruption column reaching 17 km a.s.l. in height (Firstov et al., 1994) with generation of column collapse pyroclastic flows. Lahars travelled up to 20 km along the rivers. The resulting tephra had an estimated DRE volume of $5 \times 10^6$ m$^3$ (Firstov et al., 1994). Dome growth followed the explosive eruption with peak extrusion rates of 10–14 m$^3$/s occurring in May and June 1993 (Fig. 2). The extrusion rate declined considerably by November 1993, but increased again from March 1994, with a second peak in July–October of 1994 with extrusion rates as high as 3 m$^3$/s (Fig. 2). Dome growth declined to very low values by February 1995, by which time the total dome volume was about $1.9 \times 10^8$ m$^3$. The extrusion rate thus averaged 3 m$^3$/s in the 1993–1995 eruption.

### 3.4. 1995–2001 activity

After February 1995 weak fumarolic activity was observed. The period of repose continued until 1997 when fumarole degassing became more vigorous, the first shallow earthquakes were recorded to depths of 5 km (Fedotov et al., 2001) and occasional explosions were observed. In 1998–2000 the rate of explosions increased from 7–11 to 29 per year. Starting from February 2001 the number of the explosions strongly increased, and several episodes of volcanic tremor were recorded.

## 4. The 2001–2004 eruption

The most recent eruption of Shiveluch volcano started in May 2001. Regular visual observations of a pre-eruption state had not been carried out because heavy clouds persistently obscured the volcano. Seismic data were registered by the network of the Kamchatka Experimental Methodological Seismological Department (KEMSD) and are described by Fedotov et al. (2001, 2004). Kamchatka Volcanic Eruption Response Team (KVERT) and Alaska Volcano Observatory (AVO) reports include interpretation of AVHRR satellite imagery in terms of thermal anomalies of the dome area and the distribution of ash plumes. In our description we use these sources for the reconstruction of the eruption chronology. Dome volumes were estimated from photographs taken from the town of Kluchi, approximately 40 km from the dome, and from helicopter inspections. The volumes have an estimated uncertainty of 20%.

The first signs of unrest appeared at the beginning of April 2001 when the daily numbers of earthquakes started to increase monotonically. The epicentre depths were estimated at only a few kilometres. The number of earthquakes, and amount of seismic energy released, increased strongly on April 22 and by May 200–400 earthquakes per day were counted (Fedotov et al., 2001). On 29 April the duration and intensity of swarms of volcanic tremor sharply increased and a thermal anomaly of 4 pixels was reported in satellite images by AVO on that day, marking the beginning of new dome growth. The first significant explosion occurred on 7 May, following strong, spasmodic volcanic tremor. The eruption column reached a height of 4.5 km a.s.l. and was dispersed to the northwest (Fedotov et al., 2001).

Poor weather conditions and continuous steaming at the dome area allowed visual observations to be made only on 12 May. A new dome was observed at the saddle between the 1993 dome and the 1964 crater wall (Fig. 1b) with a height of 100 m and width of 200 m (Fig. 3a). Two smaller new domes were observed, aligned roughly west–southwest–east–northeast at the northern periphery of the old dome (Fig. 1b). The volume of the new domes was determined after helicopter inspection on May 16 and amounted to $8.9 \times 10^6$, $1.4 \times 10^6$ and $1.2 \times 10^6$ m$^3$, respectively. In addition the volume of talus and proximal pyroclastic deposits around the

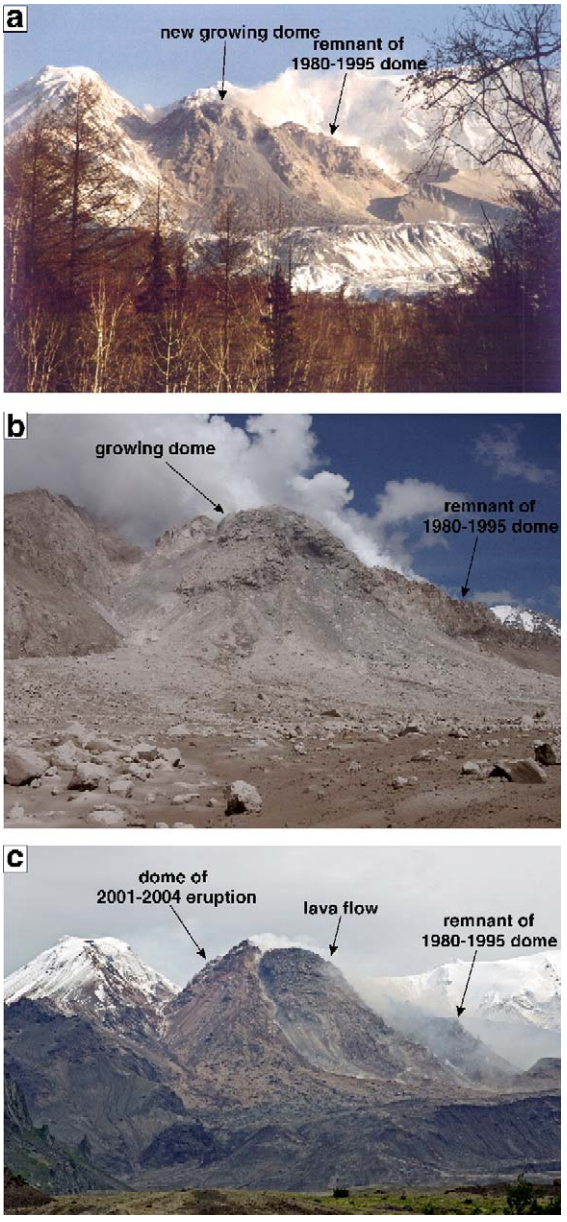


Fig. 3. Photographs of the 2001 to 2004 dome and eruption: (a) The new lava dome extrudes above the remnants of the 1980 to 1995 dome in October 2001; (b) the new dome has built over the 1980–1995 dome by July 2002; (c) in July 2004 an extrusive lobe forms a thick lava flow extruding from the summit.

domes was estimated at $3.1\times10^6\,m^3$ or $2.3\times10^6\,m^3$ DRE (Fedotov et al., 2001, 2004). The average extrusion rate over the first 16 days was thus estimated to have exceeded $11\,m^3/s$.

A decrease in volcanic tremor occurred on 14–18 May, accompanied by several weak explosions. A marked increase in volcanic tremor took place on the morning of 19 May. At 17:41 KDT (Kamchatka local time) an explosive eruption formed an eruption column, reaching a height of at least 10 km (Fedotov et al., 2001, 2004). Column collapse pyroclastic flows travelled southwest and southeast along the Baidarnaya and Kabeku rivers for at least 12 km. Visual observation revealed vigorous white steaming along these rivers consistent with interaction of the pyroclastic flows with the river and snow. A thermal anomaly at 8–10 pixels with temperatures of 30–49 °C above background levels was reported on 21 May suggesting that dome growth continued. A more powerful explosive eruption occurred at 2:09 KDT on 22 May; the eruption column reached 20 km height and spread to the south–southeast. An elongate thermal anomaly appeared that evening, suggesting the formation of pyroclastic flows. These two explosive eruptions partly destroyed the biggest of the new domes (first observed on May 12) and the western part of the 1993–1995 dome.

After these explosions dome extrusion continued and was accompanied by steaming, weak to moderate explosions, and avalanching of the dome. Between 22 May and 29 June the dome increased in height by up to 3 m per day, reaching a height of 112 m by the end of this period. The peak extrusion rate was estimated at $7\,m^3/s$ in the middle of June (Fig. 2). During this time seismic activity was above background levels. Several $M\geq2$ earthquakes, numerous small earthquakes within the volcanic edifice, local seismic signals due to explosions, avalanches, and rockfalls, and episodes of weak spasmodic volcanic tremor were recorded. Interpretation of seismic data also suggested several strong explosions during 29 June–2 July with column heights up to 8.5 km a.s.l., accompanied by formation of small pyroclastic flows. Seismicity changed on 14 July. Spasmodic volcanic tremor started to rise monotonically and its amplitude increased to $2.0\times10^{-6}$ m. In the following days the average daily amplitude of the volcanic tremor kept increasing and reached $4.0\times10^{-6}$ m by 19 July. These observations suggested a change in magma ascent regime from pulse-like to persistent growth with some oscillations in the extrusion rate (Fedotov et al., 2004).

The period of intensive dome growth with weak explosions continued until March 2002. The extrusion rate then dropped to $0.2–0.6\,m^3/s$ and dome growth soon ceased. By July 2002 the dome had buried most of the 1993–1995 dome (Fig. 3b). Extrusion then became rather stable, with slow discharge of viscous lava at the upper part of the dome, accompanied by continuous steaming, occasional rock falls from the dome and rare formation of small dome-collapse pyroclastic flows. Two short, thick lava lobes were observed at the middle part of the dome coming down from a bulge at the dome

summit. Estimates of volume in January 2003 gave about $4 \times 10^6$ m$^3$ of growth during the 10 months with an average extrusion rate of 0.2 m$^3$/s, with a small peak in November 2002 of up to 0.64 m$^3$/s.

Dome extrusion rate increased slightly in March 2003, reaching a peak of 1.5–1.6 m$^3$/s following a period of very slow dome growth with extrusion rates of 0–0.04 m$^3$/s. In March 2004 the dome continued to grow with a small peak of 0.6 m$^3$/s at the end of April. On 9 May 2004 (dashed line in Fig. 2b) another large explosive eruption occurred with the reported height of the eruption column as high as 11 km. Thereafter the style of dome activity changed from viscous dome growth to the extrusion of a less viscous lava lobe (Fig. 3c).

During the course of the 2001–2003 eruption there were over 900 explosions. Most formed eruption columns between 1 and 8 km. Rates of explosive activity remained approximately constant, albeit with minor fluctuations, between January 2002 and April 2003 and declined thereafter (Fig. 4). Rates of explosions are not correlated with rates of dome extrusion, and were maintained at a high level during a period of low extrusion rate between the peak extrusive activity.

The repose intervals between explosions were analysed using the approach of Connor et al. (2003) to investigate statistical properties of time series. This approach assumes that the time series is stationary and this is supported by nearly constant slope of the cumulative plot up to April 2003 for 750 events (Fig. 4). The detailed analysis is given in Appendix A and the results are summarised here. The repose interval data are well described by a log-logistic distribution (see Table A1 and Fig. A1), consistent with a system controlled by competing processes. Connor et al. (2003) interpret a series of Vulcanian explosions for the Soufrière Hills Volcano, Montserrat, in terms of competition of the processes that lead to an increase and decrease of gas pressure in the conduit. The Shiveluch data also suggest similar controls, but a shape parameter $k = 1–1.3$ for Shiveluch is much smaller than $k = 4$ for the Soufrière Hills Volcano. This contrast indicates less clustering for the Shiveluch data with a predominance of short repose intervals.

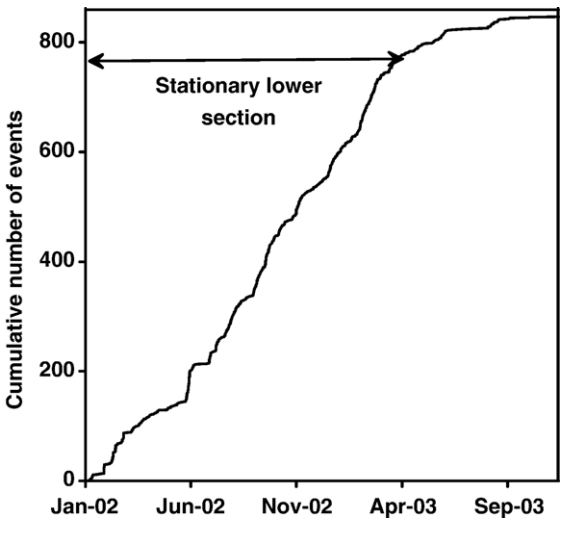


Fig. 4. Cumulative number of explosions from 4th January 2002 to 30th November 2003. The lower section of the data is stationary (i.e. it has a constant gradient on a cumulative frequency graph; see Appendix A for details).

## 5. Overall magma production 1964–2004

The total volume of the dome erupted in the periods of dome growth after the explosive eruption of 1964 to 2004 is estimated at $270 \times 10^6$ m$^3$ DRE. In addition there is a poorly constrained volume of subsidiary pyroclastic deposits related to explosive acivity. The time-averaged magma supply over the 40 years is thus at least 0.2 m$^3$/s, but the supply is strongly pulsatory. Melekestsev et al. (2004) estimated a rate of about 0.2 m$^3$/s based on studies of magma output since 970 AD. There were also shorter time-scale pulsations in the 1993 to 1995 and 2001 to 2004 dome extrusions.

## 6. Samples and analytical techniques

For petrological investigation we studied samples collected during 2002 field work at the extrusive dome carapace and from pyroclastic flow deposits of the explosive eruption on May, 2001. X-ray fluorescence (XRF) analyses were carried out using a Philips PW1400 X-ray Fluoresence spectrometer at Leicester University. Analyses of major elements were performed using fused glass discs made from powders mixed with 80:20 Li metaborate: Li tetraborate. Trace elements were determined on 32 mm, pressed powder briquettes. Electron-probe microanalysis (EPMA) was performed at the University of Bristol using a CAMECA SX-100 five spectrometer instrument. Minerals were analysed using a 20 kV accelerating voltage, 10 nA beam current and a 1–5 μm defocused beam. Groundmass glasses and melt inclusions were analysed using a 15 kV accelerating voltage, 2–4 nA beam current and a 15 μm defocused beam, with Na and Si analysed first in order to reduce the effects of alkali migration. Matrix correction was done online using a stoichiometric PAP correction (Pouchou and Pichoir, 1984). Water contents of hydrous glasses were analysed using the ‘by difference’ method

Table 1
Whole rock major and trace element contents for magmas of the 2001–2004 eruption of Shiveluch. Major element contents of previous eruptions are also shown. Data sources: 1 Tolstykh et al., 2000; 2 Bindeman et al., 2004; 3 Kepezhinskas et al., 1997; 4 Hochstaedter et al., 1996; 5 Volynets et al., 2000; 6 Pineau et al., 1999; 7 Volynets et al., 1997; 8 Popolitov and Volynets, 1982; 9 Ishikawa et al., 2001

| Sample | Reference | Date erupted | $SiO_2$ | $TiO_2$ | $Al_2O_3$ | $FeO_{tot}$ | MnO | MgO | CaO | $Na_2O$ | $K_2O$ | $P_2O_5$ | LOI | Total |
|---|---|---|---|---|---|---|---|---|---|---|---|---|---|---|
| SHV202002 | This study | July 2002 | 62.39 | 0.51 | 16.44 | 4.35 | 0.08 | 3.31 | 5.55 | 5.08 | 1.15 | 0.16 | 0.09 | 99.09 |
| SHV202003 | This study | May 2001 | 61.54 | 0.57 | 16.61 | 4.67 | 0.09 | 3.60 | 5.85 | 4.97 | 1.21 | 0.16 | 0.27 | 99.54 |
| SHIVO1/#1 | This study | May 2001 | 61.27 | 0.56 | 16.57 | 4.73 | 0.09 | 3.66 | 5.84 | 4.95 | 1.22 | 0.17 | 0.23 | 99.29 |
| SHIV01/#2 | This study | May 2001 | 61.55 | 0.55 | 16.61 | 4.73 | 0.09 | 3.65 | 5.95 | 4.97 | 1.20 | 0.17 | 0.18 | 99.66 |
| SHIV01/#3 | This study | July 2001 | 61.30 | 0.56 | 16.54 | 4.85 | 0.09 | 3.77 | 5.99 | 4.93 | 1.25 | 0.17 | 0.13 | 99.59 |
| SHIV01/#4 | This study | May 2001 | 61.81 | 0.54 | 16.26 | 4.55 | 0.09 | 3.51 | 5.71 | 4.82 | 1.17 | 0.17 | 0.34 | 98.97 |
| Av.(3) of 1995 erup. | [1] | 1995 | 60.62 | 0.57 | 16.57 | 5.00 | 0.10 | 3.99 | 5.92 | 4.58 | 1.28 | – | | 98.64 |
| Av.(2) of 1993 erup. | [1] | 1993 | 61.09 | 0.56 | 16.80 | 4.64 | 0.11 | 3.98 | 6.03 | 4.50 | 1.31 | – | | 99.01 |
| Av.(2) of 1980 erup. | [6] | 1980 | 60.33 | 0.59 | 16.62 | 5.08 | 0.11 | 4.12 | 6.16 | 4.43 | 1.24 | – | | 98.67 |
| Av.(10) of 1964 erup. | [2–4] | 1964 | 58.49 | 0.62 | 16.32 | 5.89 | 0.13 | 4.67 | 6.90 | 4.10 | 1.42 | 0.25 | | 98.78 |
| Av.(61) Shiveluch | [1–9] | | 57.02 | 0.68 | 15.93 | 6.09 | 0.12 | 6.18 | 7.15 | 3.88 | 1.31 | 0.26 | | 98.62 |

| Sample | As | Ba | Co | Cr | Cu | Ga | Mo | Nb | Ni | Pb | Rb | Sc | Sn | Sr | Th | U | V | Y | Zn | Zr |
|---|---|---|---|---|---|---|---|---|---|---|---|---|---|---|---|---|---|---|---|---|
| SHV202002 | 5.3 | 367 | 12 | 83 | 34 | 19 | 3 | 1.8 | 22 | 2.6 | 23.3 | 16 | 0 | 594 | 10.8 | 2.1 | 88 | 12 | 49 | 111 |
| SHV202003 | 5.9 | 367.2 | 15 | 90 | 35 | 18 | 2.4 | 1.9 | 26 | 5.7 | 23.0 | 14 | 3.2 | 591 | 7.2 | 0 | 97 | 15 | 52 | 112 |
| SHIVO1/#1 | 4.9 | 366.5 | 15 | 94 | 37 | 18 | 3.1 | 1.7 | 28 | 6.2 | 23.2 | 18 | 0 | 587 | 6.9 | 1.4 | 104 | 15 | 55 | 112 |
| SHIV01/#2 | 6 | 346.7 | 17 | 94 | 48 | 19 | 1.6 | 2.2 | 26 | 3 | 23.3 | 17 | 2.4 | 591 | 9.5 | 0 | 104 | 15 | 54 | 109 |
| SHIV01/#3 | 6.3 | 360.4 | 14 | 102 | 44 | 19 | 2.9 | 0 | 27 | 7 | 23.9 | 18 | 0 | 585 | 7.5 | 0 | 94 | 14 | 48 | 120 |
| SHIV01/#4 | 5.5 | 363.3 | 14 | 88 | 37 | 19 | 3.3 | 3.4 | 29 | 3.3 | 23.0 | 18 | 0 | 579 | 7.9 | 2.3 | 107 | 14 | 56 | 115 |

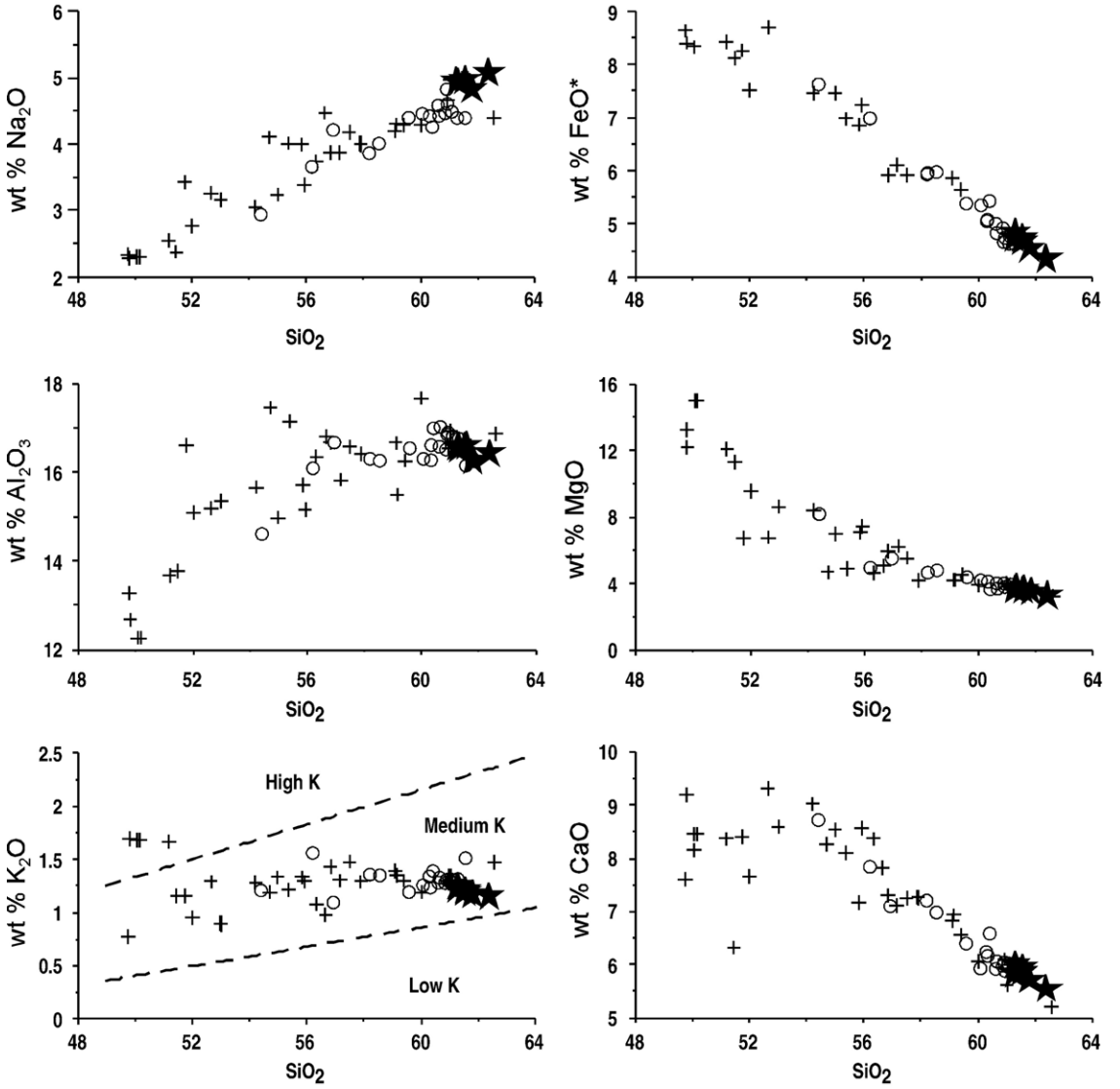


Fig. 5. Bulk rock compositions from Shiveluch volcano. Stars: 2001–2004 eruption (this work); circles: 1964–1995; crosses: all other Shiveluch eruptions. See Table 1 for other data sources.

after calibration against standard glasses with known water contents. Additionally, a subset of melt inclusions was analysed for $H_2O$ by secondary ion mass spectrometry (SIMS), using a CAMECA ims-4f instrument at the University of Edinburgh. A 5 μm, 3 nA rastered $O^-$ primary beam was accelerated onto the sample surface with a net impact energy of 14.5 kV. Secondary ions were extracted at +4.5 keV energy, with a 75 eV offset and ±20 eV energy window. Secondary $H^+$ ions were measured, and the ratio H/Si was calibrated for $H_2O$ content using a series of well-characterised, hydrous glasses after Blundy and Cashman (2005). Errors in $H_2O$ are approximately 0.1 to 0.15 wt.%. Total groundmass compositions were estimated using the scanning regime on a Camscan-4DV electron microscope with Link-10000 EDS at Moscow State University. Phenocryst-free, 100 × 150 μm areas of groundmass were analysed using a 15 kV accelerating voltage. Backscatter electron photographs were produced using a Camscan-4DV SEM (Moscow State University) or a Hitachi S-3500N SEM (University of Bristol).

## 7. Whole rock geochemistry

All the rocks collected are medium-K silicic andesites, in the classification of Gill (1981). The andesites

Table 2
Modal data for samples from the 2001–2004 eruption

| Sample | shiv01/1 Dome | shiv01/2 Pumice | shiv01/3 Dome | shiv01/3 inclusion | shiv01/4 Pumice | shv202002 Dome | shv202003 Pumice |
|---|---|---|---|---|---|---|---|
| Plagioclase | 28.8 | 15.7 | 35.2 | 44.0 | 25.1 | 18.6 | 21.6 |
| Amphibole | 14.0 | 8.3 | 14.9 | 31.7 | 9.9 | 11.6 | 8.9 |
| Orthopyroxene | 0.8 | 0.5 | 0.5 | 1.2 | 0.1 | 1.7 | 0.8 |
| Opaques | 1.7 | 0.8 | 0.9 | 4.0 | 0.8 | 0.8 | 1.6 |
| Olivine | 0.4 | 0.3 | 0.0 | 0.0 | tr | 0.3 | tr |
| Apatite | tr | tr | tr | 2.6 | 0.0 | tr | 0.0 |
| Anhydrite | 0.0 | 0.0 | 0.0 | 0.7 | 0.0 | 0.0 | 0.0 |
| Glass/groundmass | 54.1 | 74.2 | 48.3 | 15.7 | 64.0 | 66.8 | 67.0 |
| Total | 100 | 100 | 100 | 100 | 100 | 100 | 100 |
| % Crystallised | 46 | 26 | 52 | 84 | 36 | 33 | 33 |

have between 61 wt.% and 63 wt.% $SiO_2$ and plot in the calc-alkaline field of Miyashiro (1974). Representative whole rock major element analyses are given in Table 1 and compared in Fig. 5 with compositions of the 1964–1995 activity and other Young Shiveluch samples.

## 8. Andesite petrography

The andesite is highly crystalline, containing approximately 26–52 wt.% phenocrysts (Table 2), plus groundmass crystallisation. The dominant phenocryst phases are plagioclase (52–70% of phenocrysts) and amphibole (27–38%). Other phenocrysts are orthopyroxene (<1–5%) and titanomagnetite (2–5%). The groundmass comprises plagioclase, orthopyroxene, clinopyroxene and titanomagnetite, and high-$SiO_2$ rhyolite glass (77–79 wt.% anhydrous $SiO_2$). Ilmenite, cassiterite, sphene, bornite, cuprite, fluor-apatite and anhydrite are present in minor or trace amounts. Magnetite in the groundmass increases near amphibole phenocrysts and large bubbles. The bulk composition of the groundmass, estimated by SEM analysis of selected phenocryst-free areas (e.g. Fig. 6a), is given in Table 3. There are sparse olivine, clinopyroxene and Mg-rich orthopyroxene xenocrysts, which commonly have well-developed reaction rims. The samples also contain small inclusions of andesite with a diktytaxitic texture (Fig. 6b), and crystal clots (Fig. 6c).

*Plagioclase* occurs as euhedral phenocrysts up to 2.5 mm in length, microphenocrysts, microlites and inclusions in amphibole. Phenocrysts commonly contain abundant inclusions of apatite and glass, commonly arranged in concentric zones (Fig. 6d), as well as less common inclusions of amphibole, orthopyroxene and titanomagnetite. In some larger phenocrysts, amphibole inclusions are confined to the rims. This may indicate that plagioclase crystallisation started slightly earlier than amphibole. Some phenocrysts show complex oscillatory zoning, while in contrast, some are remarkably uniform in composition. In some cases oscillations are superimposed on an underlying gradual rimward decrease in $X_{An}$. In a typical sample ~10–15% of the plagioclase phenocrysts are estimated to show disequilibrium textures. For example, sieve textures (Fig. 6e), comprising a network of μm-scale melt channels, are generally confined to a narrow ring near the rim of the crystal and indicate partial dissolution (e.g. Tsuchiyama, 1985; Nakamura and Shimakita, 1998). Spongy textured crystals typically contain abundant, large, irregularly shaped melt inclusions. Plagioclase phenocrysts show a skewed, unimodal distribution of composition ranging from $An_{29}$ to $An_{74}$ (Fig. 7a). The majority of phenocryst compositions lie between $An_{36}$ and $An_{56}$, while the average groundmass plagioclase microlite has $An_{46}$–$An_{48}$ (Table 3). In oscillatory zoned crystals, oscillations have an amplitude of up to ~20% anorthite.

*Amphibole* occurs as euhedral to anhedral, strongly pleochroic phenocrysts up to 5 mm in length. Amphibole

Fig. 6. Photomicrographs and backscatter SEM photographs showing mineralogical and textural features of Shiveluch lavas. (a) Groundmass texture in dome rocks, showing strong groundmass crystallisation and some crystal alignment. (b) Quenched texture of andesitic inclusion, with randomly oriented, elongate amphibole and apatite. (c) Large crystal clot comprising small grains of plagioclase, amphibole and oxides. (d) Oscillatory zoned plagioclase containing many small melt inclusions arranged in zones (black arrows). (e) Sieve texture in plagioclase, comprising a network of fine melt channels in crystallographic orientations. (f) Large amphibole phenocryst (pale grey) with zonal arrangement of plagioclase inclusions (medium grey). (g) Amphibole rims are pristine and show no evidence of breakdown reactions. (h) Distinct rim zoning in amphibole phenocryst. Scale bars represent 100 μm, except (c) (0.5 mm).

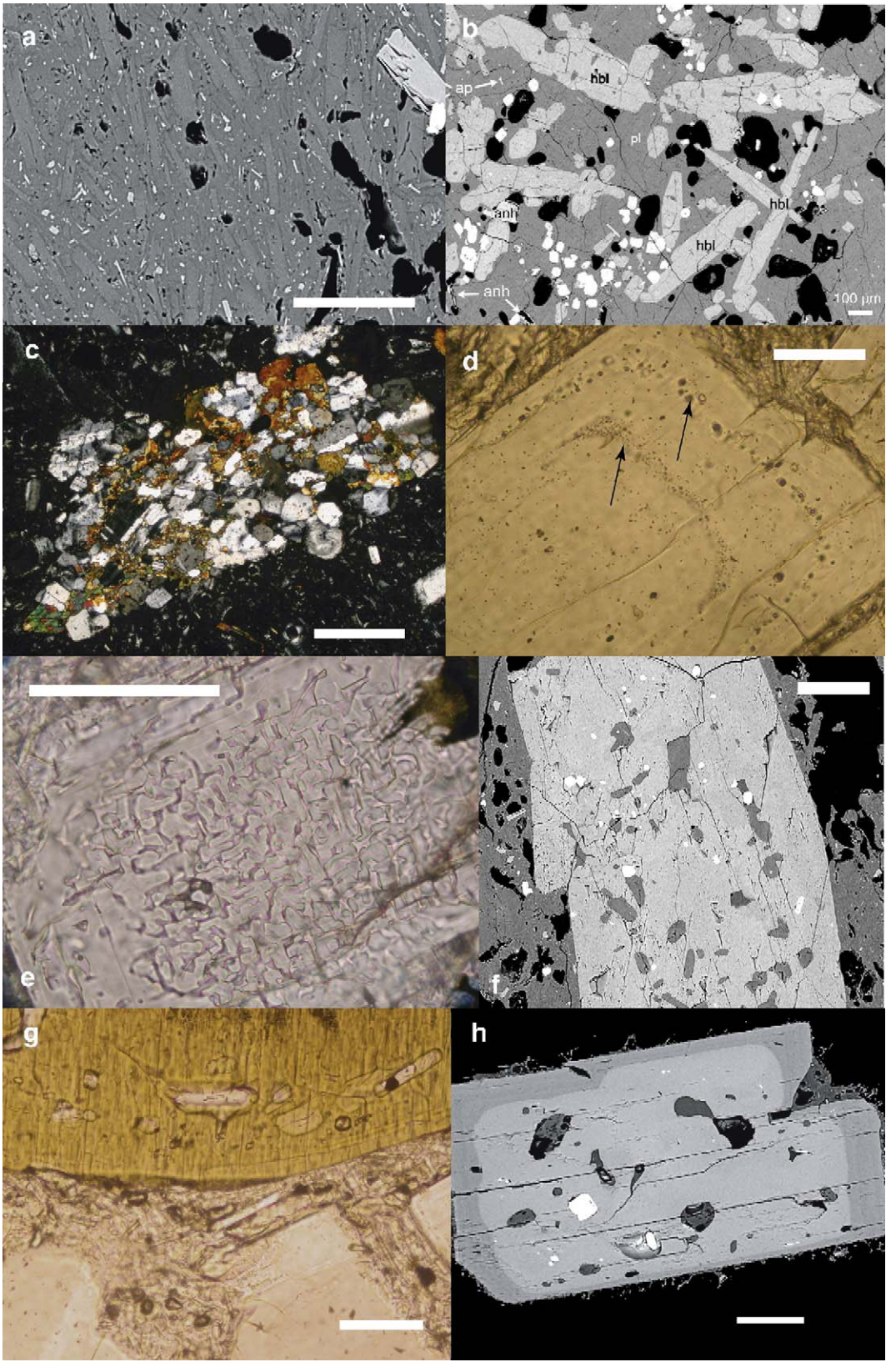
a
b
ap
hbl
pl
anh
hbl
hbl
anh
100 µm
c
d
e
f
g
h

Table 3
Variation of residual melt composition during crystallisation. Groundmass microlites are assumed to be plagioclase, orthopyroxene and clinopyroxene. Proportions of each microlite phase are estimated from the composition of the total groundmass and average phase compositions, using a least-squares method. Evolving melt compositions are calculated assuming crystallisation of this assemblage

| | Most primitive melt inclusions | Total groundmass | Average plagioclase microlites | Average clinopyroxene microlites | Average orthopyroxene microlites | 10% crystallisation | 20% crystallisation | 30% crystallisation | 40% crystallisation | Most evolved melt inclusions | Most evolved matrix glasses |
|---|---|---|---|---|---|---|---|---|---|---|---|
| $SiO_2$ | 69.93 | 68.55 | 56.83 | 52.63 | 53.99 | 70.85 | 72.60 | 74.84 | 77.84 | 79.30 | 78.40 |
| $TiO_2$ | 0.24 | 0.28 | 0.02 | 0.17 | 0.13 | 0.31 | 0.34 | 0.38 | 0.44 | 0.33 | 0.31 |
| $Al_2O_3$ | 14.95 | 16.28 | 26.45 | 1.44 | 0.72 | 15.63 | 14.56 | 13.18 | 11.34 | 10.76 | 12.16 |
| FeO | 1.44 | 1.75 | 0.56 | 7.25 | 16.97 | 1.75 | 1.72 | 1.67 | 1.62 | 1.28 | 1.08 |
| MnO | 0.05 | 0.05 | – | 0.37 | 0.92 | 0.04 | 0.03 | 0.03 | 0.02 | 0.04 | 0.04 |
| MgO | 0.41 | 0.73 | 0.13 | 15.19 | 25.31 | 0.56 | 0.33 | 0.04 | 0.00 | 0.27 | 0.12 |
| CaO | 2.46 | 3.61 | 9.21 | 21.85 | 1.31 | 3.10 | 2.40 | 1.50 | 0.30 | 0.48 | 0.66 |
| $Na_2O$ | 5.11 | 5.53 | 6.00 | 0.60 | 0.02 | 5.61 | 5.63 | 5.65 | 5.68 | 3.90 | 4.04 |
| $K_2O$ | 2.57 | 1.68 | 0.22 | – | – | 1.87 | 2.08 | 2.35 | 2.71 | 3.50 | 3.22 |
| $P_2O_5$ | 0.08 | 0.25 | – | – | – | 0.28 | 0.31 | 0.36 | 0.42 | 0.06 | 0.06 |
| $SO_2$ | 0.04 | – | – | – | – | | | | | 0.02 | 0.01 |
| Total | 99.89 | 98.65 | 99.43 | 99.50 | 99.37 | 100 | 100 | 100 | 100 | 99.96 | 100.25 |
| No. analyses | 5 | 5 | 18 | 2 | 7 | Calc | Calc | Calc | Calc | 5 | 5 |
| log($\eta$), Pa s | 9.50 | 9.03 | | | | 9.26 | 9.57 | 10.02 | 10.50 | 10.82 | 10.88 |

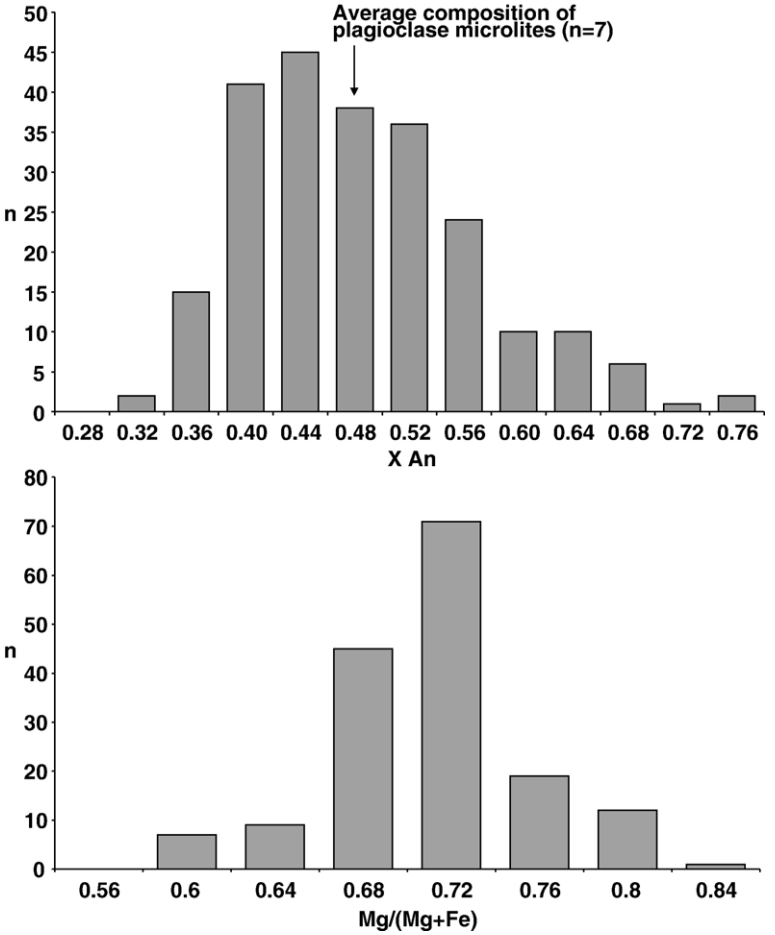


Fig. 7. Compositional variations of plagioclase (a) and amphibole (b) phenocrysts in the 2001–2003 Shiveluch eruption rocks.

contains abundant inclusions of plagioclase (both as euhedral laths and anhedral crystals), Fe–Ti oxides, pyroxenes and glass. Plagioclase inclusions are commonly concentrated in the cores (Fig 6f), consistent with plagioclase preceding amphibole in the crystallisation sequence. Some large amphibole phenocrysts have resorbed rims (but without reaction rims, Fig. 6g). The spatial distribution and proportion of inclusions varies strongly within any sample. The majority of amphiboles are unzoned, classifying as magnesiohornblendes (Leake, 1968). Mg# in amphibole has a mean of 0.72, but varies between 0.6 and 0.84 (Fig. 7b). Some crystals show a compositionally distinct, (Na, Mg, Si)-rich, (K, Ti, Fe)-poor rim (Fig. 6h). Boundaries between core and rim are crystallographically clear and there is little evidence of dissolution of the internal zones.

*Orthopyroxene* occurs as euhedral phenocrysts up to 1 mm in size. It also occurs as inclusions in amphibole and plagioclase, and as microlites together with clinopyroxene. Orthopyroxene also grows as a symplectite with magnetite replacing olivine xenocrysts. Orthopyroxene phenocrysts may contain inclusions of Fe–Ti oxides. Phenocrysts of orthopyroxene vary in composition from $En_{69–86}$ with an average of $En_{73}$ ($n=13$). Orthopyroxene inclusions within olivine, and in reaction rims on olivine, tend to be richer in Mg, with average composition $En_{84}$. Orthopyroxene xenocrysts are Mg-rich, up to $En_{90}$, and rimmed with amphibole.

*Clinopyroxene* occurs as occasional inclusions in phenocrysts, rarely as phenocrysts, and as microlites. Compositions are in the range $Wo_{43–46}$ and Mg# 0.76–0.84.

*Titanomagnetite* occurs as individual microphenocrysts and microlites, as inclusions in amphibole and pyroxene phenocrysts and as symplectites in the breakdown of olivine. In some samples, magnetite shows coarse exsolution lamellae of ülvospinel. Fe–Ti oxide phases are dominated by spinels, with only rare ilmenite. The composition of titanomagnetite ranges from 3.7 to 6.6 wt.% $TiO_2$.

*Olivine* occurs as large, subhedral to anhedral, isolated xenocrysts, commonly showing strong evidence of disequilibrium. The degree of reaction varies from crystals surrounded by a reaction corona of Fe–Ti oxides, orthopyroxene and amphibole (Fig. 8), to complete replacement by sub-grains of orthopyroxene, magnetite, amphibole and sometimes plagioclase. A sharp boundary marks the contact of the olivine and the internal part of the rim, comprising a symplectite of orthopyroxene and titanomagnetite. Amphibole forms the external part of the rim. In some cases a sharp phase boundary is observed between the internal and external parts of the rim; in others no boundary is apparent. In some cases the amphibole outer zone is itself overgrown by later amphibole which contains plagioclase and melt inclusions. Remnant olivines have composition of $Fo_{80}$–$Fo_{87}$. Enstatite-rich orthopyroxene and Mg-chromite are occasionally found as inclusions in olivine. Orthopyroxene in the reaction rims has Mg# 0.80, similar to the Mg# in the olivine.

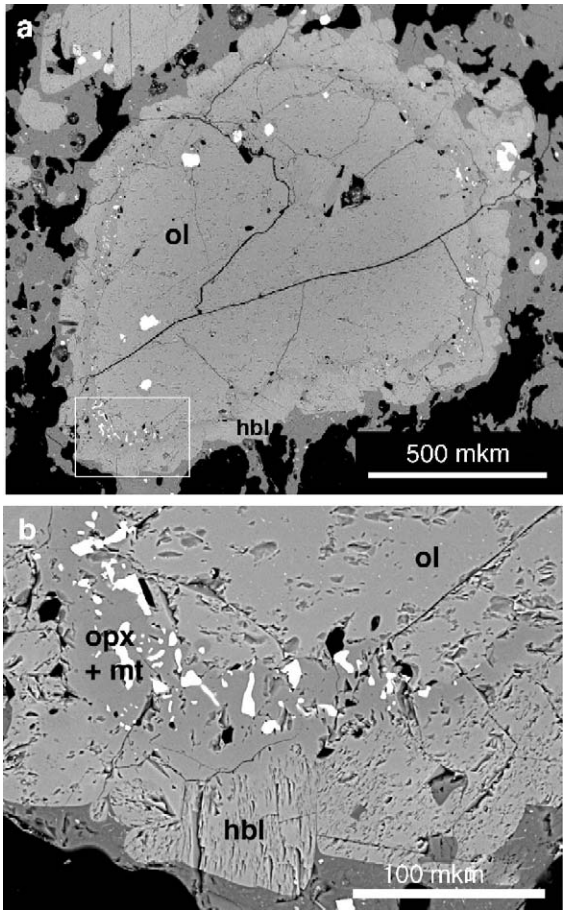


Fig. 8. (a) Olivine xenocryst with reaction rim, and (b) close-up view of rim. The rim comprises two parts: an external part of amphibole, and an internal region composed of orthopyroxene–magnetite intergrowths. The width of the internal part is nearly constant around the crystal, whereas the external part has variable width. In some areas, the amphibole outer part of the rim seems itself to be overgrown by amphibole containing plagioclase and melt inclusions.

*Melt inclusions* are abundant in amphibole and plagioclase phenocrysts. In plagioclase, the inclusions range in size from about 10 to 120 μm in size, and commonly contain fluid bubbles. In amphiboles, the size of inclusions typically ranges from 10 to 100 μm. Partial crystallisation is common in amphibole-hosted melt inclusions but less common in plagioclase-hosted inclusions. Melt inclusions in amphibole and plagioclase were analysed by EPMA and SIMS. A detailed analysis of these results will be presented elsewhere. Melt compositions show no significant difference between host phenocrysts, or with the presence or absence of bubbles. We therefore found no evidence for significant post-entrapment crystallisation of the host, and assume that the inclusions represent the original melt composition (Pletchov et al., 2005). The melt inclusions are rhyolitic in composition and form a continuous series with increasing $SiO_2$ up to the groundmass which has 77–79 wt.% $SiO_2$ (normalised to 100% anhydrous). Water contents analysed by SIMS range from 0.1 wt.% in the groundmass glass, to a maximum of 5.1 wt.% for the melt inclusions.

## 9. Magma system properties

In this section we use the petrological observations and data to make some estimates of the key properties of the Shiveluch magma system, including magma properties in the chamber and conditions during magma ascent.

### 9.1. Temperature

Magma temperatures in the Shiveluch andesite have been estimated using several approaches. The plagioclase–amphibole geothermometer of Holland and Blundy (1994) was applied to inclusions of plagioclase in amphibole as well as (less commonly) inclusions of amphibole in plagioclase. Temperatures were calculated using their Thermometer B for quartz-absent assemblages, giving temperatures accurate to ±35–40 °C. Phenocryst temperatures are quoted for a pressure of 2 kbar. The variation of the thermometer with pressure (3–4 °C per kbar) is insignificant compared with the uncertainty in the temperature estimate. Temperatures range from ~775 °C to ~940 °C, with an average of ~843 °C ($n$=76, Fig. 9). Magma temperatures were also estimated from coexisting Fe–Ti oxides using the

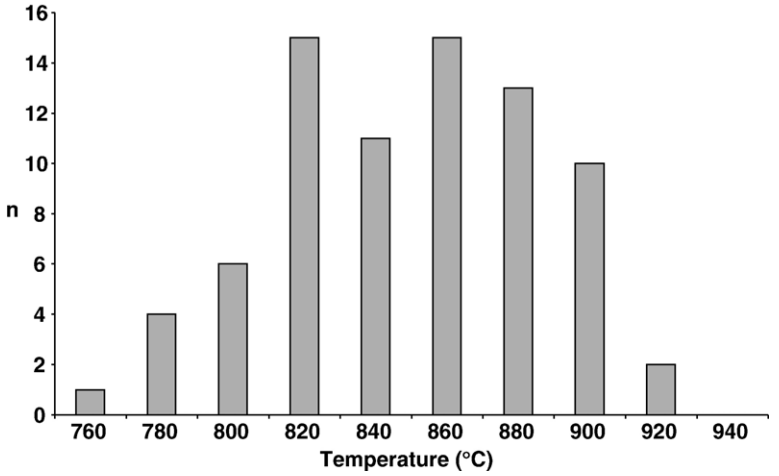


Fig. 9. Temperatures of coexisting plagioclase–amphibole pairs, calculated using Thermometer B of Holland and Blundy (1994).

method of Andersen and Lindsley (1988) and structural formulae calculated using Stormer (1983). Ilmenite–titanomagnetite pairs (inclusions within phenocrysts, and groundmass pairs) were identified that met the equilibrium conditions specified by Bacon and Hirschmann (1988). Temperatures, quoted for a pressure of 2 kbar, ranged from 834 °C to 978 °C, with an average of 878 °C. Uncertainties are approximately ±60 °C. We also estimated magma liquidus temperatures, using compositions of measured melt inclusions, oxygen fugacity near NNO to NNO+1 and pressures of 100–130 MPa, using the programme MELTS-2.04 (Ghiorso and Sack, 1995). This gives a range for the liquidus of 824–900 °C, in good agreement with the results of the two geothermometers. These temperature estimates are much lower than those reported by Tolstykh et al. (2000), who heated melt inclusions in plagioclase phenocrysts and obtained homogenisation temperatures of 970–1150 °C. These anomalously high temperatures could be explained if the melt inclusions were initially heterogeneous (contained magmatic vapour trapped with the melt inclusion), or had partially leaked volatiles, either before or during heating. Such high temperatures are also inconsistent with experimental studies of phase equilibria in silicic andesites (e.g Barclay et al., 1998; Couch et al., 2003), which show that the amphibole–plagioclase assemblage could not be stable at this determined temperature range.

### 9.2. Water content and pressure

The maximum water content measured in melt inclusions is 5.1 wt.% $H_2O$ (Humphreys et al., 2004). For a water-saturated magma, this corresponds to a water pressure of ~155 MPa at 850 °C (Newman and Lowenstern, 2002). We have not measured $CO_2$ contents of the melt inclusions; the addition of 200 ppm $CO_2$ would increase this pressure estimate by 30 MPa. Pressures would also be increased slightly by the presence of sulphur or halogen-rich gases. Occurrence of anhydrite in the groundmass is an argument for a significant role of sulphur in the magmatic system of Shiveluch volcano. This is therefore a minimum pressure estimate. The estimated water pressures are consistent with abundant amphibole, which suggests that the melt was at or near water-saturated conditions, at pressures >100 MPa based on experimental studies of silicic andesites (e.g. Barclay et al., 1998; Couch et al., 2003).

Tolstykh et al. (2000) reported that the densities of pure-$CO_2$ fluid inclusions lie in the range 0.13–0.45 g/cm$^3$ (melting temperature, $T_m$ 56.7 °C, homogenisation temperature $T_h$ (gas) 8.0–31.0 °C). They assumed temperatures of 1000–1100 °C and used this to estimate pressures of 30–160 MPa. Using our estimated range of 830–900 °C for magma temperature we recalculated the fluid inclusion data from Tolstykh et al. (2000), using the model of Span and Wagner (1996) for pure $CO_2$ inclusions. We obtained pressure estimates of 27.5–133 MPa. The upper end of these estimates agrees with the pressure estimates based on water solubility assuming saturated conditions. These pressures allow us to estimate the depth of magma chamber roof to be at 5–6 km, assuming that the magma is water saturated. If the magma is not saturated the maximum depth is unconstrained. Gorelchik et al. (1997) suggested that the magma chamber is located in the depth range of 8–25 km based on seismic investigation.

### 9.3. Timescales of magma ascent: olivine reaction rims

We use the widths of olivine reaction rims in the samples from the 2001–2003 eruption, combined with experimentally derived growth rates taken from Coombs and Gardner (2004), to constrain the timescales of magma ascent.

Reaction of olivine xenocrysts with silicic melt is well-described in island arc volcanoes (e.g. Arculus and Wills, 1980; Reagan et al., 1987; Matthews et al., 1994). Olivine xenocrysts surrounded by a corona of opx–mt symplectite, and overgrown by biotite and/or amphibole, are described at Mt. Pinatubo (Matthews et al., 1992) and at Lascar Volcano (Matthews et al., 1994). Opx–mt intergrowths are common in environments where oxidation of olivine has occurred (e.g. Ambler and Ashley, 1977; van Lamoen, 1979; Johnston and Stout, 1984). In an experimental study by Coombs and Gardner (2004), $Fo_{91}$ olivine crystals were placed into rhyolitic and rhyodacitic melt, with oxygen fugacity buffered at 0.5 to 1 log units above NNO. In most of the experiments, mono-mineralogical reaction rims were produced. More complex rims, comprising both orthopyroxene and amphibole, were produced at 885 °C and 150 MPa when olivine was in contact with rhyodacitic melt. In these experiments, amphibole was in continuous contact with olivine, with orthopyroxene microlites crystallized in the melt near the boundary. The reaction rims grow from components transferred to the melt during olivine dissolution (Coombs and Gardner, 2004). Rims comparable to those observed at Shiveluch, with an inner zone of opx–mt and outer zone of amphibole were not reproduced in these experiments.

We consider formation of the reaction rims by two different mechanisms. In the first (mechanism 1), the opx–mt symplectite may grow directly onto olivine during oxidation and reaction with a hydrous, silicic melt. Though magnetite was not observed in the experiments of Coombs and Gardner (2004), the oxygen fugacity at Shiveluch is much higher (~NNO+2, based on Fe–Ti oxide data), which would promote the formation of magnetite. The orthopyroxene is very Mg-rich, reflecting the composition of the olivine, and therefore out of equilibrium with the melt. A secondary reaction of the orthopyroxene with the melt causes the formation of amphibole, which also nucleates directly onto the reaction rim from the melt. This mechanism is supported by the sharp boundary between opx and amphibole, by the similarity of the Mg# of the olivine and opx in the reaction rim, and by the presence of distinct, late-stage overgrowths of amphibole, containing inclusions of plagioclase and some glass, on some grains (Fig. 8). However, we might expect that replacement of the opx–mt symplectite by amphibole would leave relic grains of magnetite and perhaps orthopyroxene in the amphibole rim. We might also expect to see a correlation between the widths of the internal (opx–mt) and external (hbl) rims of different grains.

The second possibility (mechanism 2) is that the reaction rim forms initially as an amphibole rim nucleated directly onto the olivine. The olivine–amphibole contact becomes unstable due to some change in the external magma conditions, and causes the olivine to break down into the opx–mt symplectite, nucleating along the olivine–amphibole interface. Olivine replacement by opx–mt therefore occurs inwards from the original amphibole–olivine contact. One problem with this theory is that the proposed reaction is a solid–solid reaction, with a presumably slow reaction rate. A second problem is that we cannot constrain the $P$–$T$–$fO_2$–$H_2O$ conditions at which the olivine–amphibole interface becomes unstable, and therefore do not know what change in these conditions might be the driving force for reaction. We suggest that olivine breaks down during ascent and during residence in the hot interior of the dome, and that the two parts of the rim reflect different processes. In the first stage, related to alteration of the xenocrysts in the magma chamber, amphibole rims grow. This requires the magma to be in the amphibole stability field. The second stage (instability of the ol–amph contact) may reflect low-pressure conditions and therefore magma ascent in the extrusive column.

Olivine reaction rims were studied in 3 samples from the 2001–2004 eruption. 2 samples were collected on July 27, 2002 from the active dome and the third was erupted on May 22, 2001. Reaction rim widths were measured linearly as described in Coombs and Gardner (2004). We measured only large crystals with clearly formed rims, as suggested in Rutherford and Hill (1993), in order to avoid sections through the bottom or top of grains. No differences in rim width beyond measurement error (see Table 4) were observed to result from crystallographic orientation. This is consistent with the observations of Coombs and Gardner (2004). The results of the measurements are shown in Table 4. Internal rims (opx–mt) are constant in width (30 to 35 μm). Total rim widths (internal+external) vary widely, from 65 to 183 μm. The consistency of the internal rim widths, and the lack of correlation between internal and external rims widths, suggests that this variation cannot be explained by variations in grain cross-section. Instead, the variation could be explained by: (i) xenocrysts being injected into the non-equilibrium environment at different times, (ii) partial dissolution or destruction of some external rims,

Table 4
Time taken to grow observed rim of orthopyroxene, magnetite and amphibole on olivine xenocrysts. Values in square brackets indicate number of measurement points on several crystals in each sample. Rim widths are measured linearly following Coombs and Gardner (2004). See text for details

| Sample name | shv202003 | shv202002 | PK-02/3a |
|---|---|---|---|
| Eruption date | 22nd May 2001 | 27th July 2002 | 27th July 2002 |
| Average internal rim width (μm) | 34.9 [12] | 30.0 [26] | 32.7 [13] |
| S.D. (μm) | 3.9 | 9.4 | 5.0 |
| Average total rim width (μm) | 182.5 [11] | 93.7 [27] | 65.9 [9] |
| S.D. (μm) | 19.9 | 14.8 | 13.8 |
| Min. growth rate ($\mu m^2\ h^{-1}$) | 1.02 | 1.02 | 1.02 |
| Max. growth rate ($\mu m^2\ h^{-1}$) | 2.95 | 2.95 | 2.95 |
| Time to grow internal rim (days) | 17–50 | 13–37 | 15–44 |
| Time to grow external rim (days) | 470–1361 | 124–358 | 61–118 |

(iii) nucleation of amphibole from the melt onto the external rim, or some combination of all these factors.

Given the uncertainty in determining growth rates, we used the experimentally determined coefficient for a rhyodacitic melt at $T=885\,°C$ and $P=150\,MPa$ ($1.02\,\mu m^2/h$) as a minimum estimate, and the growth rate of olivine reaction rims in Arenal volcano ($2.95\,\mu m^2/h$) as our maximum value (both from Coombs and Gardner, 2004). Using these values, we obtain timescales of 13–50 days for formation of the inner rim, or 61–1361 days for formation of the whole reaction rim. The interpretation of these results depends on the preferred mechanism of rim formation. The estimate of 2 months to >4 years based on total rim widths reflects the residence time of the olivine xenocrysts in the system, i.e. the time between injection of basalt and eruption, under either mechanism. This residence time suggests that influx of basaltic magma occurred on at least two occasions. Sample shv202003 was erupted in May 2001, at the beginning of the extrusive episode. Rim widths from this sample indicate magma influx 470–1361 days prior to eruption (i.e. approximately August, 1997 to February, 2000). Samples shv202002 and PK-02/3a were erupted a year later, in June 2002. Rim widths from these samples indicate magma influx 9 weeks to 1 year previously (i.e. during the current extrusive episode, June 2001 to May 2002). The value of 13–50 days, obtained from internal rim widths, is valid if mechanism 2 is operating, and reflects the length of time for which the olivine–amphibole interface was unstable, though it is not clear whether the experimentally obtained growth rate is appropriate for this solid–solid reaction. This timescale is consistent across all samples, and might represent the time of magma ascent below the amphibole stability limit (approximately 50–100 MPa).

### 9.4. Timescales of magma ascent: amphibole breakdown rims

Further constraints on timescales of magma ascent can be obtained from amphibole breakdown rims. None of the amphibole phenocrysts or microphenocrysts displays evidence of breakdown (see Fig. 6g), though some evidence of resorption can be observed. Breakdown rims of cpx + opx + plag + Ti–mt form in response to decompression crystallisation (Rutherford and Hill, 1993). Rim thickness depends on time spent outside the amphibole stability field. The rate of rim growth depends on Si diffusion rates in the melt, and therefore on magma composition and $P$, $T$ conditions (Buckley et al., 2006). Rate of rim growth also depends on the final pressure of the magma. For example, amphibole can survive without growing a reaction rim for approximately 3 weeks at 700 °C and 20 MPa, but for less than 1 day at 900 °C and 90 MPa (Buckley, 2003). Rutherford and Hill (1993) calibrated amphibole reaction rim widths for the Mount St. Helens dacite and the Montserrat andesite. Using their calibration, and assuming a temperature of ~850 °C for the Shiveluch system, magma ascent at Shiveluch is estimated to have taken less than 5–7 days. This ascent time is shorter than that estimated from internal olivine breakdown rims (using mechanism 2). Olivine breakdown via mechanism 1 is thus more consistent with the observations, since this in this mechanism, reaction occurs in the chamber where amphibole is stable.

### 9.5. Volcanological constraints on ascent times and conduit dimensions

The observations of the eruption can also provide some indications of ascent time. The first thermal anomaly was observed on 29 April 2001 and the first pumiceous explosion occurred on 19 May. This sequence is interpreted as the time between the start of lava extrusion, in which relatively dense degassed and partially crystallized magma was pushed out, and the appearance of gas-rich magma capable of explosive eruption. Once the conduit has cleared and is only occupied by fresh magma, however, the ascent time

should be reduced. The reaction rims on olivine are thought not to continue growing inside the dome, because amphibole is not stable at such low pressures. The timescale for growth of the reaction rims, under mechanism 2, is therefore approximately equivalent to the ascent time. The volume of magma discharged over 20 days between 29 April and 19 May 2001 is estimated as $13.5 \times 10^6$ (dome material only) up to $19.9 \times 10^6\,m^3$. If it is assumed that this extruded magma occupied a conduit of length 5 to 6 km then the average cross-sectional area is estimated, taking into account an uncertainty in the volume of 20%, to have been between $2250\,m^2$ and $3980\,m^2$, equivalent to a cylindrical conduit with a diameter in the range 53.5 to 71 m.

## 10. Modelling of conduit flow during dome extrusion

We now apply numerical simulations based on the conduit flow model of Melnik and Sparks (2005). Observed dome volume and extrusion rates are compared with the model output. Input parameters are listed in Table 5. When data for Shiveluch are missing the model uses parameters calibrated for the Soufrière Hills Volcano Montserrat (Melnik and Sparks, 2002, 2005). Such modelling cannot provide unique definitive results because the models are highly non-linear and so may be very sensitive to small variations in the input parameters. However, we can use the constraints provided by the volcanological observations and petrological estimates to find dynamical conditions that reproduce the observed behaviour. Also the characteristic period of pulsations is particularly sensitive to chamber volume (Barmin et al., 2002; Melnik and Sparks, 2005) so the model can be used to make an estimate of the chamber size.

Table 5
Parameters used in conduit flow simulations. The rest of the parameters have the same values as discussed in Melnik and Sparks (2005)

| Description | Value |
|---|---|
| Chamber volume | $7\,km^3$ |
| Concentration of dissolved water | 5 wt.% |
| Conduit diameter | 55 m |
| Conduit length | 5 km |
| Density of crystals | $2900\,kg\,m^{-3}$ |
| Density of the melt phase | $2400\,kg\,m^{-3}$ |
| Max. growth rate | $10^{-11}\,m\,s^{-1}$ |
| Max. nucleation rate | $10^{10}\,m^{-3}\,s^{-1}$ |
| Max. undercooling for growth | 50 °K |
| Max. undercooling for nucleation | 50 °K |
| Phenocryst size | 0.25 mm |
| Temperature in the magma chamber | 850 °C |

We model dome extrusion at Shiveluch volcano based on a transient conduit flow model (Melnik and Sparks, 2005). The model investigates magma flow in a volcanic conduit from an open-system magma chamber with replenishment from a deeper supply system. The model incorporates gas exsolution, bubble growth, gas escape through the magma, decompression induced crystallisation and rheological stiffening of the magma due to an increase in crystal content during ascent. The model consists of equations of mass conservation for melt, crystals, dissolved and exsolved gas, a momentum equation for the mixture as a whole, in which the inertial term is negligibly small and pressure drop occurs due to gravity and viscous resistance, Darcy's law for the flow of gas through a system of interconnected bubbles, and an energy equation accounting for release of latent heat of crystallisation. Mass conservation equations account for mass fluxes between components of the system due to crystallisation and gas exsolution. Following Hort (1998) crystal growth and nucleation rates were introduced as functions of undercooling, where the effective liquidus temperature depends both on concentration of dissolved gas and amount of crystallised material (Blundy and Cashman, 2001). Mass flux due to crystallisation is calculated by means of an integral equation that allows the total volume increase of growing crystals to be calculated. The presence of pre-existing phenocrysts and nucleation of microlites are taken into account. We assume that the mass transfer of dissolved gas (assumed to be water) between melt and bubbles happens quasi-statically, so that analytical solutions for the concentration gradient in a bubble shell (Navon and Lyakhovski, 1998) can be applied. The difference between the local pressure and internal pressure in the growing bubbles is not large for a slowly ascending magma. Pressure disequilibrium can therefore be neglected. All the equations describing the system were presented in Melnik and Sparks (2005), so are not reproduced here. The model is developed from Melnik and Sparks (2005) by introducing a more elaborate rheological law (as described in Appendix B).

There are no available experimental data on decompression-induced crystal growth and nucleation rates for Shiveluch magmas. We therefore use predictions of the existing crystal growth model in order to calibrate them. Shiveluch samples contain 30–60% of phenocrysts and up to 30% microlites in the groundmass. The final phenocryst radius was estimated to be 300 mm based on an average of 41 measurements of plagioclase crystal dimensions. The measurements were converted to volume assuming that the plagioclases were parallelopipeds with equal long sides, in the approximate ratio

1:8:8. The model used spherical crystals of the same volume. Due to plagioclase growth, the initial phenocryst radius must be in the range 200–250 μm. Microlites are assumed to have tablet shapes with mean radius of 21.4 μm, again calculated from microlite volume measurements. Runs of the crystal growth model with equal crystal growth rates for phenocrysts and microlites did not match the observations. The volume fraction of microlites remained much smaller than the observed values, because undercooling was strongly reduced by growth of existing phenocrysts and nucleation of new microlites was not sufficient to provide large enough surface for growth. In order to match the measurements we had to decrease crystal growth rate for phenocrysts by a factor of 2.

There are two reasons why phenocryst growth may be less efficient than microlites. First is the presence of amphibole crystals (up to 30% of phenocrysts) that do not grow during magma ascent, The second is the different shapes of the crystals. As microlites have a tablet shape the ratio of the surface to the volume for microlites is larger than for phenocrysts. In order to estimate the effect of different crystal shape we introduce the ratio $\omega = \mathrm{Surf}/\mathrm{Vol}^{2/3}$ where Surf is the surface area of the crystal and Vol is its volume. Measurements give average values of $\omega_{\mathrm{mic}} = 9.61$ and $\omega_{\mathrm{ph}} = 6.32$. These two factors allowed crystal growth rate for phenocrysts to decrease by a factor of 0.46. With the values listed in Table 5 we were able to fit measurements of the final microlite and phenocryst content and size of microlite crystals, Depending on extrusion rate in the range of 0.1 to 10 $\mathrm{m}^3/\mathrm{s}$ (typical extrusion rates during Shiveluch dome growth) the values of phenocryst content varies from 34% to 37%, and groundmass microlite content from 1% to 36.7%. The phenocryst and microlite content decreases monotonically with increase in extrusion rate.

The maximum intensity of extrusion was reached at an early stage of all three eruptions (Fig. 3). We therefore suggest that dome extrusion was initiated by high critical overpressure in the magma chamber with respect to lithostatic pressure. Depressurisation of the magma chamber occurred as a result of extrusion. Without chamber replenishment, depressurisation results in a decrease in extrusion rate (Stasiuk et al., 1993), but in open system chambers replenishment of the chamber during eruption can lead to pulsatory behaviour (Barmin et al., 2002). For the 1980–1981 eruption the monotonic decrease in extrusion rate indicates that there was little or no replenishment of the magma chamber. During 1993–1995 and 2001–2004 episodes, however, the extrusion rate fluctuated markedly, suggesting that replenishment was occurring. The influx of new magma causes an increase in magma chamber pressure, and consequent increase in extrusion rate. During the 2001–2004 eruption there were at least three peaks in extrusion rate. Replenishment of the magma chamber with new hot magma can explain the transition from lava dome extrusion to viscous lava flow that occurred on Shiveluch after 10 May 2004, and which continues now.

We simulated dome growth in 2001–2002 because this dataset is the most complete and is supported by our petrological investigations. We assume the shape of the influx curve:

$$Q_{\mathrm{in}} = Q_0 \exp\left(-\left(\frac{t-t_0}{\tau}\right)^2\right)$$

Here $Q_{\mathrm{in}}$ is the influx intensity, $Q_0$ is the maximum influx, $t$ is time, $t_0$ corresponds to the time of maximum influx, and $\tau$ is the characteristic duration of the influx. We have examined many combinations of values of these parameters within the constraints provided by the observations. The best simulation results use the following values of parameters: $Q_0 = 3.4\ \mathrm{m}^3/\mathrm{s}$ days, $t_0 = 182$ and $\tau = 115$ days. The output of the model gives a magma chamber volume of 7 $\mathrm{km}^3$ assuming a spherical chamber shape. Fig. 10a shows the dependence of extrusion rate on time and Fig 10b shows the increase in the volume of erupted material with time after 6th June 2001. The timing of magma influx can be compared with the residence time of basaltic magma in the system, as calculated from the olivine reaction rims. The sample erupted on 22nd May 2001 precedes the period of magma recharge predicted by the conduit flow model (Fig. 10a). The reaction rims on the olivine must therefore have grown in response to a previous recharge event. In contrast, the two samples erupted during July 2002 (416 days on the axis of Fig. 10) give residence times of 61–118 and 124–358 days. This would place periods of magma recharge at approximately 60–360 days (Fig. 10a). This corresponds well with the period of recharge predicted by the model.

Fig 11 shows the path of eruption on a plot of extrusion rate versus chamber pressure. The steady state solution is shown by the dashed line and shows the presence of multiple steady states for a fixed chamber pressure. In the upper regime the degree of crystallisation is insignificant because of small residence times for a parcel of magma in the conduit. Therefore, magma viscosity remains relatively small and high extrusion rates are possible. In the lower regime, magma is significantly crystallised and much more viscous than in

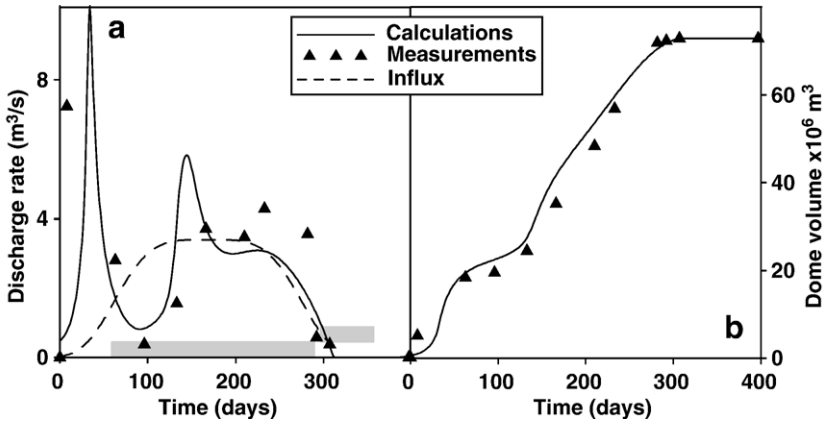


Fig. 10. (a) Comparison of calculated and measured extrusion rates (a) and volumes of the dome (b) for the episode of the dome growth in 2001–2002. Influx into the magma chamber is shown by a dashed line in (a). Time in days begins on 6th June, 2001. Samples containing olivines with reaction rims were thus erupted on Day 15 and Day 416. Grey shaded box represents the approximate timing of recharge events as inferred from olivine reaction rims. See text for details.

the upper regime. In the intermediate regime the degree of crystallinity decreases with increase in extrusion rate, leading to progressively less viscous magma. At very low discharge rates, in contrast to Melnik and Sparks (2005), chamber pressure decreases with decrease in discharge rate. This is due to a very efficient gas filtration at low magma ascent velocities, which leads to an increase of average magma density and, therefore, to increased driving pressure.

We also investigated models assuming a system of two magma chambers connected by a cylindrical conduit with a fixed flux into the deeper chamber. We were unable to match the data if the conduit between the two chambers was assumed to be rigid. In this case influx into the shallow chamber starts early in the eruption and results in a monotonic decrease in extrusion rate after the first peak. It is more plausible that the deeper supply system is connected to the peripheral magma chamber by a system of dykes that require a certain overpressure to be opened. The existing model should, therefore, be developed in order to take into account the possible elastic deformation of the deep and, possibly, shallow conduits.

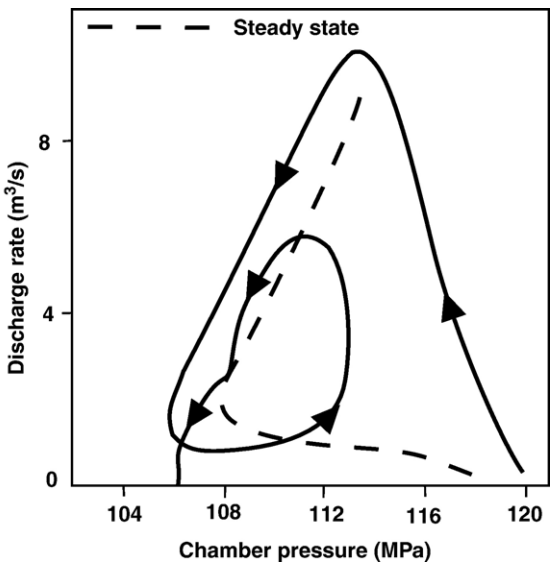


Fig. 11. Evolution of the eruption on a plot of extrusion rate vs. chamber pressure. Arrows show the direction of parameter variation with time. The steady state solution is shown by the dashed line.

## 11. Conclusions

Activity at Shiveluch volcano since the 1964 Plinian eruption has been characterised by three periods of dome growth in 1980–1981, 1993–1995 and 2001 to 2004. The last two episodes of dome growth have been marked by fluctuations in extrusion rate. Over the eruptive period about 0.27 $km^3$ of magma has extruded at a mean rate of 0.2 $m^3/s$, a result similar to the rate estimated by Melekestsev et al. (2004) for the volcano since 970 AD. Petrological and geochemical studies, together with volcanological observations, have allowed us to estimate some properties of the magma, and constrain ascent rates of magma from the shallow chamber. The temperature of the crystal-rich silicic andesite magma is estimated at approximately 850 °C from the dominant amphibole–plagioclase phenocryst assemblage and from oxide compositions. Melt inclusions in plagioclase and amphibole have up to 5.1 wt.% water, indicating a minimum chamber depth of 5 to

6 km, in agreement with estimates based on geophysical observations. Widths of reaction rims on olivine crystals are used to estimate residence times of olivine in the magma chamber. The time-scale of months to years is consistent with replenishment of the chamber from a deeper magma source during the eruption. Absence of decompression reaction rims on amphibole phenocrysts indicates ascent rates from the shallow chamber of less than a week. These mineralogical estimates are used, together with observations of extrusion rates and volumes, to estimate a conduit with a cross-section in the range 2250 $m^2$ and 3980 $m^2$, equivalent to a cylindrical conduit with a diameter in the range 53.5 to 71 m.

Using these various constraints and estimates we have applied a model of conduit flow and dome extrusion from a pressurised open-system magma chamber (Melnik and Sparks, 2005). We suggest that the eruptions were initiated by high critical overpressure in the magma chamber with respect to lithostatic pressure. Rapid depressurisation of the magma chamber occurred as a result of material evacuation at high rates. Decrease in chamber pressure led to a decrease in extrusion rate. For the 1980–1981 eruption there was no or little replenishment of the magma chamber and extrusion rate decreased monotonically. During 1993–1995 and ongoing eruptions, the course of the eruption was more complex with several smaller peaks in extrusion rate after the main peak. We suppose that depressurisation of the magma chamber led to significant replenishment from the supply system at the end of the initial pulses of dome growth. Influx of new magma during the eruption is consistent with reaction rims on olivine phenocrysts and caused the increase in magma chamber pressure, and thus increased extrusion rate. During the 2001–2004 eruption there were at least three peaks of extrusion rate which are related to magma chamber replenishment. The optimal model yields a magma chamber volume of 7 $km^3$.

## Acknowledgements

The authors acknowledge grants from INTAS (01-0106), NERC (NE/C509958/1), an international exchange grant of the Royal Society of London and the Russian Foundation for Basic Research (05-01-00228). RSJS acknowledges a Royal Society-Wolfson Award. MCSH acknowledges a NERC studentship. We thank Sergey Senukov for providing the data on explosive activity of Shiveluch volcano. The manuscript was improved by careful reviews from Michelle Coombs and Alexei Ariskin.

## Appendix A. Stochastic analysis of explosion data

We used statistical methods to analyse the time series of discrete explosions from Shiveluch volcano. Time series data were analysed using their repose intervals. The data were supplied by S. Senukov, spanning 848 days, from 4th January 2002 to 30th November 2003. We apply the approach of Connor et al. (2003), who used probabilistic methods to model 74 repose periods between Vulcanian explosions at the Soufrière Hills Volcano, Montserrat. The optimum fit to the data was found by using a log-logistic distribution. Log-logistic models have competing parameters: some parameters work to increase the probability of an event with time, while others act to decrease the probability. The model of Connor et al. (2003) had a physical foundation, based on competing processes within the conduit: pressurisation by rheological stiffening and exsolution of gas from supersaturated melts, and depressurisation by coalescence of gas bubbles and the development of fracture networks. Because there is a physical understanding of the processes driving the model, log-logistic models may have a wide application as an eruption-forecasting tool.

The two models for the statistical distribution of repose periods between explosions are the Weibull and log-logistic. The Weibull distribution can describe a classic failure model where the probability of another eruption increases with time and failure is inevitable (Voight, 1988). Connor et al. (2003) showed that the log-logistic distribution can describe a system where there are competing processes that increase and reduce pressure. The survivor function, ST($t$), gives the probability, $P$, of a repose interval, $T$, exceeding some time, $t$:

$$\mathrm{ST}(t) = P[T > t]$$

The survivor function can be expanded and applied to different probability distributions. In this study the Weibull and log-logistic distributions were compared. The Weibull survivor function is given as: $\mathrm{ST}(t) = \exp\,[-(t/\mu)^k]$, the log-logistic: $\mathrm{ST}(t) = 1/(1+(t/\mu)^k)$, where $t$ is the repose interval (time since the start of the last eruption), $\mu$ is the median repose time and $k$ is a function that changes the shape of the distribution.

For applications of this approach the series should be stationary. This is because the stochastic models (log-logistic and Weibull) use rank ordered data. A stationary series and a non-stationary series, with the same data values (but arranged differently), would yield the same results, but with different physical implications. Stationarity is displayed by a distribution that does not cluster

in time, and can be identified by a straight line on a cumulative frequency plot. Overall, the Shiveluch data indicate a non-stationary system (Fig. 4). However, the lower part (below 750 events) shows good stationarity. This stationary section was interpreted independently of the whole, non-stationary dataset.

The best-fit log-logistic and Weibull models were found (Fig. A1 and Table A1). Probability distribution fits were attempted for all the data, and for the stationary lower section (Fig. 4). A log-logistic model applied to all the data, gave a best fit by eye of $k=1.3$, but the fit that produces the least squares error is for $k=1$. The reason for this variation in optimum $k$ values is that most of the data forms very short repose intervals, so $k$ is biased towards short repose intervals. The $k=1.3$ value is an overall fit for the whole dataset including the tail. The Weibull model gave a less close fit, with the optimum value of $k=1$. The median was found to be 6.79 h.

When the data are plotted and the optimum log-logistic or Weibull value is applied to each shorter section of the data (section length is determined by how far the applied curve fits for), the log-logistic model still gave a better fit to the majority of the data, but the Weibull model fits short repose data (less than 8 h) with $k=1$ (i.e. Poisson behaviour).

Analysis of the stationary section of Shiveluch data, for the first 750 events, gave an overall good log-logistic fit of $k=1.2$, while the Weibull fit was less good. The short repose data (less than 11 h) gave a log-logistic fit ($k=1$) and a Weibull fit ($k=1$). The central section of the stationary data fits a log-logistic model of $k=1.3$. The tail (greater than 80 h), however, is purely a Weibull fit of $k=0.5$.

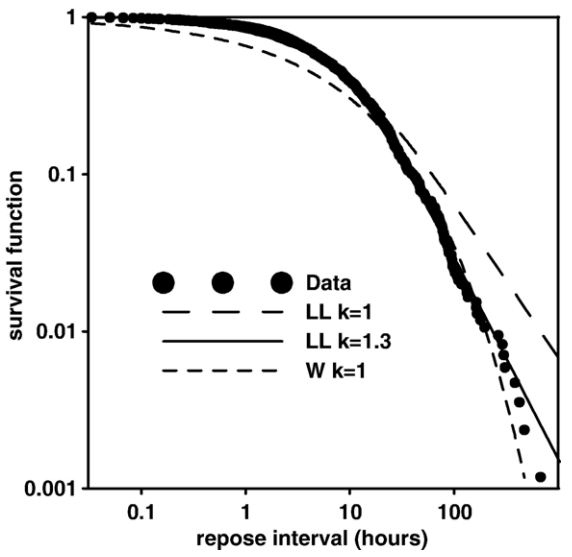


Fig. A1. Best fits for the survival function using log-logistic (LL) and Weibull distributions for repose periods between explosions from 4th January 2002 to 30th November 2003.

Table A1
Comparison of different fits for the repose interval between Vulcanian explosions

| Log-logistic or Weibull | $k$ value | Sum of squares error |
|---|---|---|
| *All data* | | |
| Log-logistic | 1 | 0.000512991 |
| Log-logistic | 1.3 | 0.001529307 |
| Weibull | 1 | 0.017428222 |
| *0–750 events* | | |
| Log-logistic | 1 | 0.000566 |
| Log-logistic | 2 | 0.009992 |
| Log-logistic | 1.2 | 0.001316 |
| Weibull | 0.5 | 0.015773 |
| Weibull | 1 | 0.012275 |

Analysis of explosion repose data from the Soufrière Hills volcano resulted in a $k$ value of 4, significantly higher than that for either Colima ($k=1.27$) (K.T. Martin, personal communication), Sakurajima ($k=1.1$ to 1.3), or Shiveluch ($k=1.3$). Most graphs appear to have 'migrating' data, i.e. the data initially follows one $k$ value, then changes to a different value for longer repose intervals. A possible reason for this changing $k$ value could be that some physical process within the volcano is changing, perhaps the conduit flow rate, and so changing the $k$ value. Alternatively it could be that on a short time scale the volcano has different dominant processes to those prevalent on a longer repose time scale. The physical implications of the parameter $k$ are currently unknown, but are the subject of work in progress. However, it is possible that $k$ may be connected to the physical properties of the magma, e.g. viscosity.

Autocorrelation describes how well the data replicates itself over a certain 'lag' period, i.e. if the same patterns are repeated again and again in time, or not. A high correlation function value (higher than 90 or 95% confidence bounds) suggests a periodicity of that interval. Autocorrelation analysis of Shiveluch volcano led to a very strong (>99% confidence) correlation at 112 day lag time. This time scale corresponds closely to seismic records, which show a periodicity approximately every 50 days, in phase with the 112 day cycles (Slezin, personal communication).

Shiveluch volcano is well described by a log-logistic distribution on varying timescales. Above 8 h repose, the data show nearly wholly log-logistic fit, implying that the system is controlled by competing processes, perhaps within the conduit. Very short repose periods

(0–3 h) displays Poisson (random) behaviour, which suggests that the system is totally random and explosions occur randomly and so cannot be forecasted. Shiveluch showed periodic behaviour, peaking in activity every 112 days.

## Appendix B. Magma rheology

One of the key features of the conduit flow model is to account for rheological changes during magma ascent. The magma is a three-component system containing melt, crystals (phenocrysts and microlites) and a free gas phase in bubbles. The main difference between the model applied here and that described in Melnik and Sparks (2005) is a more advanced rheological model as described here.

### *B.1. Melt viscosity*

Melt viscosity depends on water content, temperature and major element composition. We have used two methods of estimating melt composition prior to the magma ascent. The first takes the composition of the most primitive melt inclusions. These inclusions have low $SiO_2$, low $K_2O$ and are the richest in $H_2O$, and therefore represent the magma at the base of the conduit. In the second method we subtracted groundmass microlites from analyses of total groundmass. The proportion of microlites in the mixture was calculated from groundmass and microlite compositions using mass-balance equations and a least squares method. Both methods give similar melt compositions for the initial melt (Table 3).

Viscosities were calculated for 850 °C using the model of Giordano and Dingwell (2003), which takes into account the melt composition for dry systems. For the water and temperature dependence of viscosity the model by Hess and Dingwell (1996) is used. During crystallisation, melt viscosity increases because the chemical composition of the residual melt becomes progressively silica-reach. Estimates of melt composition at different stages of crystallisation (Table 3) allow changes in viscosity to be calculated using Giordano and Dingwell (2003). The best fit for the data is given by:

$$\mu_m = \frac{\mu_{HD}(c,T)}{\mu_{HD}(c_a,T)} 10^{(9.02+1.88\beta+4.55\beta^2)}$$

Here $\mu_{HD}$ is the viscosity model from Hess and Dingwell (1996) for the melt phase, $c$ is the mass concentration of dissolved water, $c_a$ is its value at atmospheric pressure, $T$ is the temperature, and $\beta$ is the crystal content.

### *B.2. Influence of crystals*

The following relationship is commonly used to estimate the effects of crystal content on the mixture viscosity

$$\frac{\mu_{cm}}{\mu_m} = (1-\varepsilon\beta)^{-2.5} \quad \text{(B1)}$$

where $\mu_{cm}$ is the viscosity of the crystal–melt suspension, and ε is an empirical constant. This relationship, after Marsh (1981), gives reasonable agreement with observations for $\varepsilon \approx 1.67$ and crystal contents up to about $\beta = 0.55$. However this relationship cannot be extended to the very high crystal contents, since viscosity becomes

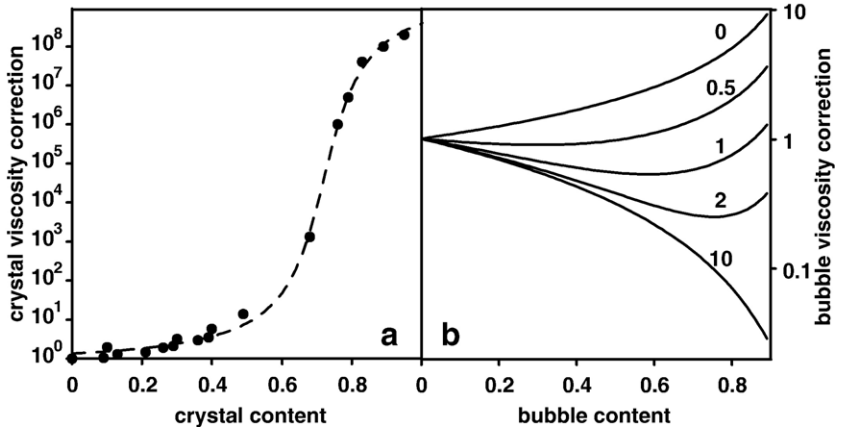


Fig. B1. (a) Relative viscosity for different crystal content (see Appendix B for the data source references). (b) Influence of capillary number (labelled on the curves) on the relative viscosity for different bubble contents.

infinite at $\beta=0.599$. Therefore, we use a modified approximation that remains finite for all values of $\beta$ following Melnik and Sparks (1999):

$$\log_{10}\left(\frac{\mu_{cm}}{\mu_m}\right) = A\arctan(B(\beta-\beta_*))-C \quad \text{(B2)}$$

Effective relative viscosities deduced by A. Costa from van der Molen and Paterson (1979) at high solid fraction, from Lejeune and Richet (1995) and Thomas (1965) at low and intermediate solid fractions. The best fit parameters in Eq. (B2) for this dataset are given by $A=3.1$, $B=11.6$, $\beta_*=0.72$ and $C=4.64$. A comparison of these viscosity models is shown in Fig. B1a.

### *B.3. Influence of bubbles*

The presence of bubbles can significantly change the viscosity of the magma (Llewellin and Manga, 2005). At low shear rates bubbles remain nearly spherical and, therefore, resist shearing. In this case, viscosity increases with increasing bubble content $\alpha$. At high shear rates bubbles are highly deformed and produce slip surfaces. This leads to a decrease in viscosity with increasing bubble content. These two regimes are distinguished by capillary number $\mathrm{Ca}=\mu_m\alpha\dot{\gamma}/\sigma$. Here $a$ is the bubble radius, $\dot{\gamma}$ is the strain rate, $\sigma$ is the surface tension. For $\mathrm{Ca}\ll 1$ the first regime is realised, for $\mathrm{Ca}\gg 1$—the second. Llewellin and Manga (2005) suggest the following approximations for the relative viscosity $\mu_r$ (the ratio of mixture viscosity and melt viscosity) of a bubbly magma:

$$\mu_r = \begin{cases} \mu_1 = (1-\alpha)^{-1}, \mathrm{Ca}\ll 1 \\ \mu_2 = (1-\alpha)^{\frac{5}{3}}, \mathrm{Ca}\gg 1 \end{cases}$$

Capillary number is related to magma extrusion rate and can vary from values much smaller than one to large values. Eq. (5) from Llewellin and Manga (2005) allows us to find the value of the relative viscosity in the intermediate range of capillary numbers, but it is difficult to use because it requires the solution of a transcendental equation. Instead we approximate $\mu_r$ by:

$$\mu_r(\mathrm{Ca},\alpha) = \frac{\mu_1(\alpha)}{1+\varsigma\mathrm{Ca}^2} + \frac{\mu_2(\alpha)\varsigma\mathrm{Ca}^2}{1+\varsigma\mathrm{Ca}^2}$$

where $\varsigma=25$ was chosen for the fit. Dependence of $\mu_r$ on $\alpha$ for different values of capillary number is shown in Fig. B1b. The viscosity of the mixture is calculated as a product of the melt–crystal viscosity and the relative viscosity due to the presence of bubble phase.

$$\mu = \mu_{mc}(c,T,\beta)\mu_r(\mathrm{Ca},\alpha)$$

## References


Ambler, E.P., Ashley, P.M., 1977. Vermicular orthopyroxene–magnetite symplectites from the Wateranga layered mafic intrusion, Queensland, Australia. Lithos 10, 163–172.

Andersen, D.J., Lindsley, D.H., 1988. Internally consistent solution models for Fe–Mg–Mn–Ti oxides–Fe–Ti–oxides. American Mineralogist 73, 714–726.

Arculus, R.J., Wills, K.J.A., 1980. The petrology of plutonic blocks and inclusions from the Lesser Antilles Island Arc. Journal of Petrology 21 (4), 743–799.

Bacon, C.R., Hirschmann, M.M., 1988. Mg/Mn partitioning as a test for equilibrium between coexisting oxides. American Mineralogist 73, 57–61.

Barclay, J., Rutherford, M.J., Carroll, M.R., Murphy, M.D., Devine, J.D., Gardner, J.E., Sparks, R.S.J., 1998. Experimental phase equilibria constraints on pre-eruptive storage conditions of the Soufriere Hills magma. Geophysical Research Letters 25, 3437–3440.

Barmin, A., Melnik, O., Sparks, R.S.J., 2002. Periodic behavior in lava dome eruptions. Earth and Planetary Science Letters 199 (1–2), 173–184.

Belousov, A.B., 1995. The Shiveluch volcanic eruption of 12 November 1964—explosive eruption provoked by failure of the edifice. Journal of Volcanology and Geothermal Research 66, 357–365.

Belousov, A., Belousova, M., Voight, B., 1999. Multiple edifice failures, debris avalanches and associated eruptions in the Holocene history of Shiveluch volcano, Kamchatka, Russia. Bulletin of Volcanology 61 (5), 324–342.

Bindeman, I.N., Ponomareva, V.V., Bailey, J.C., Valley, J.W., 2004. Volcanic arc of Kamchatka: a province with high-delta O-18 magma sources and large-scale O-18/O-16 depletion of the upper crust. Geochimica et Cosmochimica Acta 68 (4), 841–865.

Blundy, J., Cashman, K.V., 2001. Magma ascent and crystallization at Mount St Helens. Contributions to Mineralogy and Petrology 140, 631–650.

Blundy, J., Cashman, K., 2005. Rapid decompression-driven crystallization recorded by melt inclusions from Mount St. Helens volcano. Geology 33 (10), 793–796.

Braitseva, O.A., Melekestsev, I.V., Ponomareva, V.V., Sulerzhitsky, L.D., 1995. The ages of calderas, large explosive craters and active volcanoes in the Kurile–Kamchatka region, Russia. Bulletin of Volcanology 57 (6), 383–402.

Braitseva, O.A., Ponomareva, V.V., Sulerzhitsky, L.D., Melekestsev, I.V., Bailey, J., 1997a. Holocene key-marker tephra layers in Kamchatka, Russia. Quaternary Research 47 (2), 125–139.

Braitseva, O.A., Sulerzhitsky, L.D., Ponomareva, V.V., Melekestsev, I.V., 1997b. Geochronology of the greatest Holocene explosive eruptions in Kamchatka and their imprint on the Greenland glacier shield. Transaction (Doklady) Russian Academy of Science, Earth Science Section 352 (1), 138–140 (in Russian).

Buckley, V.J.E., 2003. Hornblende dehydration during magma decompression. Unpublished PhD thesis, University of Bristol.

Buckley, V.J.E., Sparks, R.S.J., Wood, B.J., 2006. Amphibole dehydration reactions during magma ascent at Soufrière Hills Volcano, Montserrat. Contributions to Mineralogy and Petrology 151 (2), 121–140.

Connor, C.B., Sparks, R.S.J., Mason, R.M., Bonadonna, C., Young, S.R., 2003. Exploring links between physical and probabilistic models of volcanic eruptions: The Soufrière Hills Volcano, Montserrat. Geophysical Research Letters 30, 1697–1701.

Coombs, M.L., Gardner, J.E., 2004. Reaction rim growth on olivine in silicic melts: Implications for magma mixing. American Mineralogist 89, 748–759.

Couch, S., Harford, C.L., Sparks, R.S.J., Carroll, M.R., 2003. Experimental constraints on the conditions of formation of highly calcic plagioclase microlites at the Soufirre Hills volcano, Montserrat. Journal of Petrology 44, 1455–1475.

Fedotov, S.A., Dvigalo, V.N., Zharinov, N.A., Ivanov, V.V., Seliverstov, N.I., Khubunaya, S.A., Demyanchuk, Yu.V., Markov, L.G., Osipenko, L.G., Smelov, N.P., 2001. The eruption of Shiveluch volcano on May–July 2001. Volcanology and Seismology 6, 3–15 (in Russian).

Fedotov, S.A., Zharinov, N.A., Dvigalo, V.N., Seliverstov, N.I., Khubunaya, S.A., 2004. Eruptive cycle of Shiveluch volcano in 2001–2004. Volcanology and Seismology 6, 3–14 (in Russian).

Firstov, P.P., Gavrilov, V.A., Zhadnova, E.Yu., Kiriyanov, V.Yu., 1994. Onset of new extrusive eruption of Shiveluch in April 1993. Volcanology and Seismology 4–5, 33–47 (in Russian).

Ghiorso, M.S., Sack, R.O., 1995. Chemical mass transfer in magmatic processes. IV. A revised and internally consistent thermodynamic model for the interpolation and extrapolation of liquid–solid equilibria in magmatic systems at elevated temperatures and pressures. Contributions to Mineralogy and Petrology 119, 197–212.

Gill, J.B., 1981. Orogenic Andesites and Plate Tectonics. Springer-Verlag, Berlin, pp. 1–390.

Giordano, D., Dingwell, D.B., 2003. Non-Arrhenian multicomponent melt viscosity: a model. Earth and Planetary Science Letters 208 (3–4), 337–349.

Gorelchik, V.I., Shirokov, V.A., Firstov, P.P., Chubarova, O.S., 1997. Shiveluch volcano: seismicity, deep structure and forecasting eruptions (Kamchatka). Journal of Volcanology and Geothermal Research 78, 121–132.

Hess, K.U., Dingwell, D.B., 1996. Viscosities of hydrous leucogranite melts: a non-Arrhenian model. American Mineralogist 81, 1297–1300.

Hochstaedter, A.G., Kepezhinskas, P., Defant, M., Drummond, M., Koloskov, A., 1996. Insights into the volcanic arc mantle wedge from magnesian lavas from the Kamchatka arc. Journal of Geophysical Research-Solid Earth 101 (B1), 697–712.

Holland, T., Blundy, J.D., 1994. Non-ideal interactions in calcic amphiboles and their bearing on amphibole-plagioclase thermometry. Contributions to Mineralogy and Petrology 116, 443–447.

Hort, M., 1998. Abrupt change in magma liquidus temperature because of volatile loss or magma mixing: effects of nucleation, crystal growth and thermal history of the magma. Journal of Petrology 39, 1063–1076.

Humphreys, M.C.S., Blundy, J., Sparks, S., 2004. Analysis of melt inclusions from Shiveluch Volcano, Kamchatka: Degassing-induced crystallisation. Abstract from IAVCEI General Assembly: Volcanism and its Impact on Society. .

Ishikawa, T., Tera, F., Nakazawa, T., 2001. Boron isotope and trace element systematics of the three volcanic zones in the Kamchatka arc. Geochimica et Cosmochimica Acta 65 (24), 4523–4537.

Johnston, A.D., Stout, J.H., 1984. Development of orthopyroxene-Fe/Mg ferrite symplectites by continuous olivine oxidation. Contributions to Mineralogy and Petrology 88, 196–202.

Kepezhinskas, P., McDermott, F., Defant, M.J., Hochstaedter, A., Drummond, M.S., Hawkesworth, C.J., Koloskov, A., Maury, R.C., Bellon, H., 1997. Trace element and Sr–Nd–Pb isotopic constraints on a three-component model of Kamchatka arc petrogenesis. Geochimica et Cosmochimica Acta 61 (3), 577–600.

Leake, B.E., 1968. Nomenclature of amphiboles. Mineralogical Magazine 42, 533–563.

Lejeune, A., Richet, P., 1995. Rheology of crystal-bearing silicate melts: An experimental study at high viscosity. Journal of Geophysical Research 100, 4215–4229.

Llewellin, E.W., Manga, M., 2005. Bubble suspension rheology and implications for conduit-flow. Journal of Volcanology and Geothermal Research 143 (1−3), 205–217.

Marsh, B.D., 1981. On crystallinity, probability of occurrence and rheology of lava and magma. Contribution to Mineralogy and Petrology 78, 85–98.

Matthews, S.J., Jones, A.P., Bristow, C.S., 1992. A simple magma-mixing model for sulphur behaviour in calc-alkaline volcanic rocks: mineralogical evidence from Mount Pinatubo 1991 eruption. Journal of the Geological Society 149, 863–866.

Matthews, S.J., Jones, A.P., Gardeweg, M.C., 1994. Lascar Volcano, northern Chile: Evidence for steady-state disequilibrium. Journal of Petrology 35 (2), 401–432.

Melekestsev, I.V., Volynets, O.N., Ermakov, V.A., Kirsanova, T.P., Masurenkov, Yu.P., 1991. Shiveluch Volcano. In: Fedotov, S.A., Masurenkov, Yu.P. (Eds.), Active Volcanoes of Kamchatka, vol. 1. Nauka, Moscow, pp. 84–92 (in Russian, summary in English).

Melekestsev, I.V., Dvigalo, V.N., Kirsanova, T.P., Ponomareva, V. V., Pevzner, M.M., 2004. 300 years of Kamchatka volcanoes life: Young Shiveluch (analysis of dynamics and consequences of eruptive activity during XVII–XX centures), part II—1965–2000 AD eruptions. Volcanology and Seismology 1, 1–20 (in Russian).

Melnik, O.E., Sparks, R.S.J., 1999. Non-linear dynamics of lava dome extrusion. Nature 402, 37–41.

Melnik, O., Sparks, R.S.J., 2002. The dynamics of magma ascent and lava extrusion at the Soufrière Hills Volcano, Montserrat. In: Druitt, T.H., Kokelaar, B.P. (Eds.), The Eruption of Soufrière Hills Volcano, Montserrat, from 1995 to 1999. Geological Society of London, Memoir, vol. 21, pp. 153–171 (London).

Melnik, O., Sparks, R.S.J., 2005. Controls on conduit magma flow dynamics during lava dome building eruptions. Journal of Geophysical Research 110 (B02209), doi:10.1029/2004JB003183.

Menyailov, A.A., 1955. Shiveluch volcano, its geological structure, composition and eruptions. Trans Volcan Lab USSR Acad Sci 9 (in Russian).

Miyashiro, A., 1974. Volcanic rock series in island arcs and active continental margins. American Journal of Science 274, 321–355.

Nakamura, M., Shimakita, S., 1998. Dissolution origin and syn-entrapment compositional change of melt inclusion in plagioclase. Earth and Planetary Science Letters 161, 119–133.

Navon, O., Lyakhovski, V., 1998. Vesiculation processes in silicic magmas. In: Gilbert, J.S., Sparks, R.S.J. (Eds.), Physics of Explosive Eruptions. The Geological Society, London, pp. 27–50.

Newman, S., Lowenstern, J.B., 2002. VolatileCalc: a silicate melt–$H_2O$–$CO_2$ solution model written in Visual Basic for Excel. Computers and Geosciences 28, 597–604.

Pevzner, M.M., Ponomareva, V.V., Melekestsev, I.V., 1998. Cherny Yar: reference section of the Holocene marker ash layers for the NE

coast of Kamchatka. Volcanology and Seismology 19, 389–406 (in Russian).

Pineau, F., Semet, M.P., Grassineau, N., Okrugin, V.M., Javoy, M., 1999. The genesis of the stable isotope (O, H) record in arc magmas: the Kamtchatka's case. Chemical Geology 153 (1–4), 93–124.

Pletchov, P.Yu., Puzankov, M.Yu., Dirksen, O.V., Latyshev, N.P., 2005. Constraints to Shiveluch extrusive dome growth. Abstracts of Petrography Symposium, Apatity.

Ponomareva, V.V., Pevzner, M.M., Melekestsev, I.V., 1998. Large debris avalanches and associated eruptions in the Holocene eruptive history of Shiveluch Volcano, Kamchatka, Russia. Bulletin of Volcanology 59 (7), 490–505.

Popolitov, E.I., Volynets, O.N., 1982. Geochemistry of quarternary volcanic rocks from the Kurile–Kamchatka island arc. Journal of Volcanology and Geothermal Research 12 (3–4), 299–316.

Pouchou, J.L., Pichoir, F., 1984. PAP ($\phi$–$\rho$–$z$) correction procedure for improved quantitative microanalysis. In: Armstrong, J.T. (Ed.), Microbeam Analysis. San Francisco Press, California, pp. 104–106.

Reagan, M.K., Gill, J.B., Malavassi, E., Garcia, M.O., 1987. Changes in magma composition at Arenal volcano, Costa Rica, 1968–1985: Real-time monitoring of open-system differentiation. Bulletin of Volcanology 49, 415–434.

Rutherford, M.J., Hill, P.M., 1993. Magma ascent rates from amphibole breakdown: An experimental study applied to the 1980–1986 Mount St. Helens eruption. Journal of Geophysical Research 98, 19667–19685.

Span, R., Wagner, W., 1996. A new equation of state for carbon dioxide covering the fluid region from the triple-point temperature to 100 K at pressures up to 800 MPa. Journal of Physical and Chemical Reference Data 25 (6), 1509–1596.

Stasiuk, M.V., Jaupart, C., Sparks, R.S.J., 1993. Variations of flow rate and volume during eruption of lava. Earth and Planetary Science Letters 114, 505–516.

Thomas, D., 1965. Transport characteristics of suspensions: VIII. A note on the viscosity of Newtonian suspensions of uniform spherical particles. Journal of Colloidal Sciences 20, 267–277.

Tolstykh, M.L., Naumov, V.B., Babanskii, A.D., Khubunaya, S.A., Kononkova, N.N., 2000. Chemical composition, trace elements, and volatile components of melt inclusions in minerals from andesites of the Shiveluch volcano, Kamchatka. Geochemistry International 38, 123–132.

Tsuchiyama, A., 1985. Dissolution kinetics of plagioclase in the melt of the system diopside–albite–anorthite, and origin of dusty plagioclase in andesites. Contributions to Mineralogy and Petrology 89, 1–16.

van der Molen, I., Paterson, M., 1979. Experimental deformation of partially melted granite. Contributions to Mineralogy and Petrology 70, 299–318.

van Lamoen, H., 1979. Coronas in olivine gabbros and iron ores from Susimaki and Riuttamaa, Finland. Contributions to Mineralogy and Petrology 68, 259–268.

Voight, B., 1988. A method for prediction of volcanic eruptions. Nature 332, 125–130.

Volynets, O.N., Ponomareva, V.V., Babansky, A.D., 1997. Magnesian basalts of Shiveluch andesite volcano, Kamchatka. Petrology 5 (2), 183–196.

Volynets, O.N., Babanskii, A.D., Gol'tsman, Y.V., 2000. Variations in isotopic and trace-element composition of lavas from volcanoes of the Northern group, Kamchatka, in relation to specific features of subduction. Geochemistry International 38 (10), 974–989.

Zharinov, N.A., Bogoyavlenskaya, G.E., Khubunaya, S.A., Demyanchuk, Yu.V., 1995. New eruptive cycle on Shiveluch volcano—1980–1993. Volcanology and Seismology 1, 20–28 (in Russian).